

Small-scale and large-scale intermittency in the nocturnal boundary layer and the residual layer

By ANDREAS MUSCHINSKI¹†, ROD G. FREHLICH²
AND BEN B. BALSLEY²

¹CIRES, University of Colorado and NOAA Environmental Technology Laboratory,
325 Broadway, R/ET2, Boulder, Colorado 80305-3328, USA

²CIRES, University of Colorado, Campus Box 216, Boulder, Colorado 80309, USA

(Received 11 September 2003 and in revised form 6 May 2004)

In high Reynolds-number turbulence, local scalar turbulence structure parameters, $(C_\theta^2)_r$, local scalar variance dissipation rates, χ_r , and local energy dissipation rates, ε_r , vary randomly in time and space. This variability, commonly referred to as intermittency, is known to increase with decreasing r , where r is the linear dimension of the local averaging volume. Statistical relationships between χ_r , ε_r , and $(C_\theta^2)_r$ are of practical interest, for example, in optical and radar remote sensing. Some of these relationships are studied here, both theoretically and on the basis of recent observations. Two models for the conditionally averaged local temperature structure parameter, $\langle (C_\theta^2)_r | \varepsilon_r \rangle$, are derived. The first model assumes that the joint probability density function (j.p.d.f.) of χ_r and ε_r is bivariate lognormal and that the Obukhov–Corrsin relationship, $(C_\theta^2)_r = \gamma \varepsilon_r^{-1/3} \chi_r$, where $\gamma = 1.6$, is locally valid. In the second model, small-scale intermittency is ignored and C_θ^2 and ε are treated traditionally, that is, as averages over many outer scale lengths, such that C_θ^2 and ε change only as a result of large-scale intermittency. Both models lead to power-law relationships of the form $\langle (C_\theta^2)_r | \varepsilon_r \rangle = c \varepsilon_r^\delta$, where c is a constant. Both models make predictions for the value of the power-law exponent δ . The first model leads to $\delta = \rho_{xy} \sigma_y / \sigma_x - 1/3$, where σ_x and σ_y are the standard deviations of the logarithms of ε_r and χ_r , respectively, and ρ_{xy} is the correlation coefficient of the logarithms of χ_r and ε_r . This model leads to $\delta = 1/3$ if $\rho_{xy} = 2/3$ and if $\sigma_x = \sigma_y$. The second model predicts $\delta = 2/3$, regardless of whether (i) static stability and shear are statistically independent, or (ii) they are connected through a Richardson-number criterion. These theoretical predictions are compared to fine-wire measurements that were taken during the night of 20/21 October 1999, at altitudes of up to 500 m in the nocturnal boundary layer and the overlying residual layer above Kansas. The fine-wire sensors were moved up and down with the University of Colorado’s Tethered Lifting System (TLS). The data were obtained during the Cooperative Atmosphere–Surface Exchange Study 1999 (CASES-99). An interesting side result is that the observed frequency spectra of the logarithms of ε_r and χ_r are described well by an f^{-1} law. A simple theoretical explanation is offered.

† Present address: Electrical and Computer Engineering Department, University of Massachusetts, Knowles Building, 151 Holdsworth Way, Amherst, MA 01003-9284, USA

1. Introduction

Atmospheric turbulence occurs at time and length scales that range over many orders of magnitude. Obukhov (1962) suggested distinguishing between small-scale turbulence and large-scale turbulence, where small scales are scales at which “the hypothesis of three-dimensional isotropy is valid in a certain rough approximation”, and large scales are those at which the fluctuations are necessarily anisotropic because beyond a certain scale, atmospheric flow is always quasi-two-dimensional.

Now, let L be the diameter of the largest turbulent eddies that are still part of the small-scale turbulence. That length scale is known variously as the ‘outer scale’, ‘large-eddy scale’, or ‘overturning length’. In the vicinity of the ground or a wall, L is of the order of the distance between the observation point and the boundary. At higher levels in the atmosphere, the small-scale turbulence does not ‘feel’ the presence of the ground, and L is determined by the local mean vertical gradient of the potential temperature and the local mean vertical shear of horizontal velocity.

Large-scale turbulence (mesoscale variability, gravity waves, or synoptic-scale disturbances) is known to have drastic effects on the statistical parameters of the small-scale turbulence. Randomness in small-scale turbulence statistics is generally referred to as intermittency. It is important, however, to distinguish between the intermittency that is an inherent part of small-scale turbulence (Kolmogorov 1962; Obukhov 1962) and the intermittency that is associated with, and caused by, large-scale variability of the flow. The problem of distinguishing between the two does not arise in wind-tunnel experiments because large-scale turbulence simply does not exist there. As pointed out by Obukhov (1962, p. 78): “In the study of turbulence in wind tunnels one usually takes averages over a certain ensemble corresponding to a time ensemble, and the averaging period is larger than the life-time of the largest eddies. In the case of atmospheric turbulence there arise specific difficulties; so that the life-time of the largest eddies in the atmosphere greatly exceeds, as a rule, the time of measuring turbulent characteristics.”

In the turbulence literature, the term ‘intermittency’ has been used more broadly than outlined above, and with different meanings that vary across authors and disciplines. Intermittency has been defined or characterized simply as “another name for nonstationarity” (Treviño & Andreas 2000) or as “an unexpected high probability of large velocity fluctuations” (Boettcher *et al.* 2003). Sreenivasan (1999, p. S389) defines turbulence intermittency as the non-Gaussianity of small-scale statistics: “Roughly speaking, intermittency means that extreme events are far more probable than can be expected from Gaussian statistics and that the probability density functions of increasingly smaller scales are increasingly non-Gaussian . . .”

Sreenivasan & Antonia (1997, p. 441) divide small-scale intermittency into dissipation-scale intermittency and inertial-range intermittency: “Batchelor & Townsend (1949) showed that the non-Gaussian behavior in the pdf of dissipation quantities increased with decreasing scale. In a complementary sense, dissipation quantities become increasingly non-Gaussian as the Reynolds number increases. These are the two hallmarks of dissipation-scale intermittency. For the inertial range, since the Reynolds number variation should be irrelevant, intermittency requires that the pdfs of wavenumber bands show increasingly flared-out tails for increasing midband wavenumber, or that the flatness of velocity increments increases with decreasing scale.” Mahrt (1989) distinguishes between “small scale or microscale intermittency” and “global intermittency”. This is exactly what we will refer to here as small-scale intermittency and large-scale intermittency, respectively.

For many years, clear-air Doppler radars have been used to remotely sense energy dissipation rates and refractive-index structure parameters in the troposphere and the stratosphere (e.g. VanZandt *et al.* 1978; Gage 1990; Nastrom & Eaton 1997; Doviak & Zrnić 1993; Muschinski & Lenschow 2001). Clear-air radar data are usually processed with averaging times ranging from minutes to hours and with averaging volumes with diameters ranging from tens of metres to a few kilometres. Recently, Muschinski (2004) generalized the existing theory of clear-air radio-wave backscatter and analysed the effects of spatial and temporal variability of local turbulence statistics within the radar’s resolution volume and during the radar’s dwell time. There is a similar interest in small-scale intermittency in the area of optical remote sensing (e.g. Frehlich 1992; Wheelon 2001, 2003).

In this study, we investigate both small-scale and large-scale intermittency in the nocturnal boundary layer (NBL) and in the lower part of the residual layer (RL). We analyse measurements collected with vertical arrays of fine-wire anemometers and thermometers lifted to altitudes as much as 500 m above ground level. The data were taken on 21 October 1999 during Intensive Observational Period 9 (IOP 9) of the month-long field campaign of the Cooperative Atmosphere-Surface Exchange Study 1999 (CASES-99) conducted near Leon, Kansas (Poulos *et al.* 2002).

2. Small-scale turbulence and small-scale intermittency

2.1. Small-scale turbulence

One of the main goals of understanding small-scale turbulence is to establish laws for the statistical properties of two-point velocity increments,

$$\Delta \mathbf{u} \equiv \mathbf{u}(\mathbf{x}'', t) - \mathbf{u}(\mathbf{x}', t), \tag{2.1}$$

where \mathbf{u} is the local and instantaneous velocity vector, and \mathbf{x}' and \mathbf{x}'' are two fixed locations.

An important working assumption is that in a space–time domain \mathcal{D} whose spatial dimensions are sufficiently small, the statistical properties of $\Delta \mathbf{u}$ are nearly homogeneous, isotropic, and stationary. In other words, the statistics of $\Delta \mathbf{u}$ are assumed to be independent of time t , independent of the mid-point location $\mathbf{x} \equiv (\mathbf{x}' + \mathbf{x}'')/2$, and independent of the orientation of the separation vector $\mathbf{s} \equiv \mathbf{x}'' - \mathbf{x}'$, such that the statistics are functions only of the magnitude $s \equiv |\mathbf{s}|$ of the separation vector. Mid-point and separation coordinates had already been used by Tatarskii (1961). The advantage of using mid-point and separation coordinates instead of using the ‘end-point coordinates’ \mathbf{x}' and \mathbf{x}'' were recently discussed by Hill & Wilczak (2001).

According to classical turbulence theory (Kolmogorov 1941), any $\Delta \mathbf{u}$ statistic for a given \mathcal{D} should depend only on the molecular kinematic viscosity ν and on the average value of the energy dissipation rate, ε , over that specific domain \mathcal{D} (Kolmogorov’s first similarity hypothesis). Furthermore, in the inertial range, i.e. for r large compared to the dissipation length, or Kolmogorov microscale,

$$\eta = \left(\frac{\nu^3}{\varepsilon} \right)^{1/4}, \tag{2.2}$$

but still small compared to the outer length scale L , any $\Delta \mathbf{u}$ statistic should be independent of ν and depend solely on ε (Kolmogorov’s second similarity hypothesis).

In a broader sense, turbulence is also randomness in the field of a scalar variable, θ , like temperature, humidity, refractive index, etc. We refer to such turbulence as ‘scalar turbulence’ as opposed to ‘velocity turbulence’. The functional form of the

second-order structure function of scalar increments

$$\Delta\theta \equiv \theta(\mathbf{x}'', t) - \theta(\mathbf{x}', t) \quad (2.3)$$

in the inertial subrange was predicted by Obukhov (1949) and Corrsin (1951).

2.2. Small-scale intermittency

In their refined similarity theory, Kolmogorov (1962) and Obukhov (1962) introduced local averages ε_r over (small) spheres with radius $r \ll L$. They assumed that ε_r is lognormally distributed and that the variance σ_x^2 of the logarithm of ε_r increases with decreasing r like

$$\sigma_x^2 = A + \mu \ln \frac{L}{r}, \quad (2.4)$$

where μ is a universal constant and the coefficient A “depends on the macrostructure of the flow” (Kolmogorov 1962, p. 83). Equation (2.4), together with the lognormality assumption, is sometimes referred to as Kolmogorov’s third similarity hypothesis (e.g. Sreenivasan, Antonia & Danh 1977).

Van Atta (1971) hypothesized, firstly, that local averages χ_r of scalar variance dissipation rates should be lognormally distributed and that the variance σ_y^2 of the logarithm of χ_r increases with decreasing r :

$$\sigma_y^2 = A_\theta + \mu_\theta \ln \frac{L_\theta}{r}, \quad (2.5)$$

where L_θ and μ_θ are the scalar counterparts of L and μ , respectively. Secondly, Van Atta (1971) hypothesized that the joint probability of ε_r and χ_r should be bivariate lognormal. It is natural to assume that L and L_θ are of comparable magnitude. Relationships resulting from the joint lognormality hypothesis are summarized in Antonia & Van Atta (1975). A review on intermittency in passive-scalar turbulence was given by Warhaft (2000).

3. Fine-wire measurements of local dissipation rates and structure parameters: concepts and procedures

Local dissipation rates can be retrieved from fine-wire measurements by means of two different techniques: the direct dissipation technique and the inertial-range technique. Both retrieval techniques rely on a number of assumptions. An outline is given in the following.

For incompressible, Newtonian fluids at high Reynolds numbers, ε_r and χ_r are given by

$$\varepsilon_r = \left\langle \frac{\nu}{2} \sum_{i=1}^3 \sum_{j=1}^3 \left(\frac{\partial u_i}{\partial x_j} + \frac{\partial u_j}{\partial x_i} \right)^2 \right\rangle_r \quad (3.1)$$

(e.g. Taylor 1935, equation 41 on p. 436) and

$$\chi_r = \left\langle 2\kappa \sum_{i=1}^3 \left(\frac{\partial \theta}{\partial x_i} \right)^2 \right\rangle_r \quad (3.2)$$

(e.g. Sreenivasan 1996), where u_i and u_j are the i th and j th, respectively, components of the fluctuating part of the velocity vector, θ is the fluctuating part of the temperature, and κ is the molecular heat conductivity. The spatial averaging, denoted by $\langle \cdot \rangle_r$, is performed over a domain of linear size r . Kolmogorov (1962) specified the averaging volume as a sphere with radius r .

With a single fine wire, however, only fluctuations in the streamwise direction can be measured, such that (3.1) and (3.2) cannot be directly applied for two reasons: first, a fine wire measures only fluctuations along a line, which makes averaging over volumes impossible; second, (3.1) and (3.2) also involve gradients in the transverse directions, which cannot be measured with a single fine wire.

It is commonly assumed that the shape of the averaging volume is of minor importance (Monin & Yaglom 1975, p. 591) and that it is only the linear dimension r of the averaging domain that matters. Under these assumptions, volume averaging can be replaced by line averaging. Moreover, it is commonly assumed that the fluctuations are statistically isotropic at scales comparable to the Kolmogorov length, which makes direct measurement of the transverse gradients unnecessary because in that case (3.1) and (3.2) are equivalent to

$$\varepsilon_r = 15\nu \left\langle \left(\frac{\partial u_1}{\partial x_1} \right)^2 \right\rangle_r \tag{3.3}$$

(first derived by Taylor 1935, equation 45 on p. 437) and

$$\chi_r = 6\kappa \left\langle \left(\frac{\partial \theta}{\partial x_1} \right)^2 \right\rangle_r, \tag{3.4}$$

respectively, where ‘1’ stands for the streamwise direction.

Because fine wires measure time series and not spatial series, a local version of Taylor’s frozen-turbulence hypothesis has to be used to retrieve streamwise gradients from time derivatives:

$$\varepsilon_r = 15 \frac{\nu}{U_r^2} \left\langle \left(\frac{\partial u_1}{\partial t} \right)^2 \right\rangle_\tau \tag{3.5}$$

and

$$\chi_r = 6 \frac{\kappa}{U_r^2} \left\langle \left(\frac{\partial \theta}{\partial t} \right)^2 \right\rangle_\tau. \tag{3.6}$$

Here, U_r is the true air speed (i.e. the magnitude of the sensor’s velocity vector relative to the air) averaged over the time period τ . For a given τ , we have $r = U_r \tau$. If the fluctuations of the true air velocity vector during τ are significant compared to U_r , then Taylor’s hypothesis in its original form (Taylor 1938) may lead to serious overestimations of $\langle (\partial u_1 / \partial x_1)^2 \rangle$ and $\langle (\partial \theta / \partial x_1)^2 \rangle$ and, therefore, of energy and scalar variance dissipation rates. Equations to quantify and correct biases resulting from the original, i.e. ‘global’, Taylor hypothesis (Taylor 1938) have been worked out, e.g., by Heskestad (1965), Lumley (1965) and Wyngaard & Clifford (1977). Wyngaard & Clifford (1977) found that global energy dissipation rates are overestimated by $15 \langle u_1^2 \rangle / U^2$ and global temperature variance dissipation rates by $9 \langle u_1^2 \rangle / U^2$, where U is the global mean true air speed and $\langle u_1^2 \rangle$ is the global variance of the streamwise velocity. These results have been confirmed by Hill (1996).

Correspondingly, the local version of Taylor’s hypothesis, which is also known as the ‘random Taylor hypothesis’ (e.g. Tennekes 1975) or ‘sweeping decorrelation hypothesis’ (Praskovsky *et al.* 1993), leads to overestimations by $15 \langle u_1^2 \rangle_r / U_r^2$ in ε_r and by $9 \langle u_1^2 \rangle_r / U_r^2$ in χ_r , where $\langle u_1^2 \rangle_r$ is the local variance of the streamwise velocity. Because $\langle u_1^2 \rangle_r / \langle u_1^2 \rangle$ is of order $(r/L)^{2/3}$, the biases resulting from the local Taylor hypothesis are only of order $15 \langle u_1^2 \rangle (r/L)^{2/3} / U^2$ and $9 \langle u_1^2 \rangle (r/L)^{2/3} / U^2$, respectively.

In summary, (3.5) and (3.6) rely on the following three assumptions: (i) negligibility of the shape of the local averaging volume; (ii) statistical isotropy at length scales comparable to the Kolmogorov length; and (iii) the validity of the local Taylor hypothesis. Although errors resulting from violations of one or more of these three assumptions may lead to significant biases, measurements of ε_r and χ_r by means of (3.5) and (3.6) are usually, and somewhat misleadingly, called ‘direct’ dissipation measurements.

Direct dissipation measurements in high-Reynolds-number flows require extremely high spatial and temporal resolution. According to Kuznetsov, Praskovsky & Sabelnikov (1992, p. 602), the spatial resolution has to be 2η or better, which translates into the following requirement for the time resolution:

$$\Delta t \leq \frac{2}{U_r} \left(\frac{\nu^3}{\varepsilon_r} \right)^{1/4}. \quad (3.7)$$

(Muschinski (1996) pointed out that there is a relationship between this ‘ 2η criterion’ and the requirement that the Smagorinsky coefficient in large-eddy simulations must exceed a certain critical value.) In the NBL, a typical wind speed is 10 m s^{-1} and one has to be prepared for local values of the energy dissipation rate as large as $0.1 \text{ m}^2 \text{ s}^{-3}$. With $\nu = 1.5 \times 10^{-5} \text{ m}^2 \text{ s}^{-1}$ this leads to $2\eta = 0.86 \text{ mm}$ and $\Delta t \leq 86 \mu\text{s}$. That is, the sampling rate has to be 11.7 kHz or higher. Although this is feasible – Kuznetsov *et al.* (1992), for example, sampled wind-tunnel turbulence at 32 kHz – the difficulties associated with direct dissipation measurements in the open atmosphere, particularly onboard airborne platforms, usually do not justify the expenses.

As an alternative to the direct dissipation technique, one can retrieve dissipation rates with the inertial-range technique. As described in the following, local structure parameters are extracted from the inertial subrange of the measured spectra, and dissipation rates are then computed from the structure parameters.

Local structure functions for streamwise velocity and for temperature are defined by

$$D_{11}^{(r)}(s) = \langle [u(x + s/2) - u(x - s/2)]^2 \rangle_r, \quad (3.8)$$

and

$$D_{\theta\theta}^{(r)}(s) = \langle [\theta(x + s/2) - \theta(x - s/2)]^2 \rangle_r, \quad (3.9)$$

respectively. Here, s is the separation in the streamwise direction, and $\langle \cdot \rangle_r$ means that the structure functions are estimated from spatial series of length r . In the inertial range, the structure functions follow the two-thirds laws

$$D_{11}^{(r)}(s) = (C_u^2)_r s^{2/3} \quad (3.10)$$

and

$$D_{\theta\theta}^{(r)}(s) = (C_\theta^2)_r s^{2/3}, \quad (3.11)$$

where $(C_u^2)_r$ is the local structure parameter of streamwise velocity and $(C_\theta^2)_r$ is the local temperature structure parameter. The corresponding local, one-sided, one-dimensional, streamwise wavenumber spectra are

$$F_{11}^{(r)}(k_1) = \frac{2}{3\Gamma(1/3)} (C_u^2)_r k_1^{-5/3} \quad (3.12)$$

and

$$F_{\theta\theta}^{(r)}(k_1) = \frac{2}{3\Gamma(1/3)} (C_\theta^2)_r k_1^{-5/3}, \quad (3.13)$$

where $2/3\Gamma(1/3) = 0.2489$. Inertial-range theory for velocity turbulence (Kolmogorov 1941; Obukhov 1941*a, b*) and for scalar turbulence (Obukhov 1949; Corrsin 1951) leads to

$$F_{11}^{(r)}(k_1) = \alpha_1 \varepsilon_r^{2/3} k_1^{-5/3} \tag{3.14}$$

and

$$F_{\theta\theta}^{(r)}(k_1) = \gamma \varepsilon_r^{-1/3} \chi_r k_1^{-5/3}. \tag{3.15}$$

The Kolmogorov coefficient α_1 is quasi-universal and has a value close to 0.5 (Yaglom 1981; Sreenivasan 1995; Gotoh, Fukayama & Nakano 2002). The Obukhov–Corrsin coefficient γ is also quasi-universal and has a value close to 0.4 (Sreenivasan 1996). This leads to

$$(C_u^2)_r = 2.0 \varepsilon_r^{2/3} \tag{3.16}$$

and

$$(C_\theta^2)_r = 1.6 \varepsilon_r^{-1/3} \chi_r, \tag{3.17}$$

respectively.

Usually, the local wavenumber spectra $F_{11}^{(r)}(k_1)$ and $F_{\theta\theta}^{(r)}(k_1)$ are not directly measured but are, by means of the local Taylor hypothesis, obtained from the one-sided, local frequency spectra $S_{11}^{(r)}(f)$ and $S_{\theta\theta}^{(r)}(f)$. The relationships are

$$F_{11}^{(r)}(k_1) = \frac{U_r}{2\pi} S_{11}^{(r)}(f) \tag{3.18}$$

and

$$F_{\theta\theta}^{(r)}(k_1) = \frac{U_r}{2\pi} S_{\theta\theta}^{(r)}(f), \tag{3.19}$$

respectively, where

$$f = \frac{U_r}{2\pi} k_1 \tag{3.20}$$

is frequency.

The inertial-range technique relies on the following assumptions: (i) negligibility of the shape of the local averaging volume; (ii) statistical isotropy in the wavenumber range within which the model spectrum is fitted to the measured spectrum; (iii) the existence of inertial subranges in the velocity and temperature fields; (iv) the assumptions that the inertial-subrange theories are locally valid and that the Kolmogorov and Obukhov–Corrsin coefficients are universal and known; and (v) the validity of the local Taylor hypothesis.

The ε_r and χ_r data that will be analysed in the following were obtained with the inertial-range technique. The measured spectra were fitted to refined models for $F_{11}^{(r)}(k_1)$ and $F_{\theta\theta}^{(r)}(k_1)$, respectively. These models account for the ‘Hill bump’ (Hill 1978) in the scalar spectrum, the drop-off of spectral density at wavenumbers where dissipation is no longer negligible, and white noise in the sensors. A detailed description of the models and the estimation algorithms was given by Frehlich *et al.* (2003).

Because the measurements were made in the stably stratified atmosphere, the turbulence intensities $\sqrt{\langle u_1^2 \rangle}_r / U_r$ were very small compared to 1, such that errors caused by the local Taylor hypothesis were negligible and no correction was made.

4. Two theoretical models of conditionally averaged local turbulence statistics

One purpose of this study is to analyse and theoretically explain observations of $\langle (C_\theta^2)_r | \varepsilon_r \rangle$, that is, of conditional averages of $(C_\theta^2)_r$ for fixed values of ε_r . We

will see that the observed values of $\langle (C_\theta^2)_r | \varepsilon_r \rangle$ are proportional to ε_r^δ , where δ is a numerical exponent. The main two questions that we will address are: First, is the power-law behaviour of $\langle (C_\theta^2)_r | \varepsilon_r \rangle$ a consequence of the lognormality of small-scale intermittency statistics, or can it be explained within the framework of classical concepts of turbulence? Second, what is the physics behind the power-law exponent δ ?

We will present two different theoretical models of $\langle (C_\theta^2)_r | \varepsilon_r \rangle$. The first model builds on the joint lognormality assumption for small-scale intermittency. The second model ignores small-scale intermittency entirely and, instead, explains $\langle C_\theta^2 | \varepsilon \rangle$ on the basis of simple mixing-length arguments. (Note that in the second scenario we have suppressed the suffix r because, in that case, the size of the averaging volume plays no role in the theory. It is only assumed that the averaging volume is large compared to L .)

Although these two theoretical concepts have very little in common, both lead to power laws for $\langle (C_\theta^2)_r | \varepsilon_r \rangle$ and $\langle C_\theta^2 | \varepsilon \rangle$, respectively.

4.1. The small-scale intermittency model

Let us assume that the joint lognormality hypothesis (Van Atta 1971; Antonia & Van Atta 1975) is valid, such that the joint probability density function (j.p.d.f.) of χ_r and ε_r is

$$p(\varepsilon_r, \chi_r) = \frac{1}{2\pi\varepsilon_r\chi_r\sigma_x\sigma_y\sqrt{1-\rho_{xy}^2}} \exp \left\{ -\frac{\frac{x^2}{\sigma_x^2} - 2\rho_{xy}\frac{x}{\sigma_x}\frac{y}{\sigma_y} + \frac{y^2}{\sigma_y^2}}{2(1-\rho_{xy}^2)} \right\}, \quad (4.1)$$

where

$$x = \ln \frac{\varepsilon_r}{\bar{\varepsilon}_r} \quad (4.2)$$

is the (natural) logarithm of the normalized energy dissipation rate ε_r ($\bar{\varepsilon}_r$ is chosen such that $\langle \ln(\varepsilon_r/\bar{\varepsilon}_r) \rangle = 0$), with σ_x as the standard deviation of x ,

$$y = \ln \frac{\chi_r}{\bar{\chi}_r} \quad (4.3)$$

is the logarithm of the normalized temperature variance dissipation rate, χ_r ($\bar{\chi}_r$ is chosen such that $\langle \ln(\chi_r/\bar{\chi}_r) \rangle = 0$), with σ_y as the standard deviation of y , and

$$\rho_{xy} = \frac{\langle xy \rangle}{\sigma_x\sigma_y} \quad (4.4)$$

is the correlation coefficient of x and y .

Let us follow Peltier & Wyngaard (1995, p. 3642) and assume that the Corrsin (1951) relationship,

$$C_\theta^2 = \gamma\varepsilon^{-1/3}\chi, \quad (4.5)$$

is locally valid, such that

$$(C_\theta^2)_r = \gamma\varepsilon_r^{-1/3}\chi_r, \quad (4.6)$$

where the Obukhov–Corrsin coefficient γ is assumed to have a universal value close to 1.6, and that γ does not vary with r ; see also (3.17).

The conditional average of $(C_\theta^2)_r$ for a fixed value of ε_r is

$$\langle (C_\theta^2)_r | \varepsilon_r \rangle = \frac{\int p(\chi_r, \varepsilon_r) \gamma \varepsilon_r^{-1/3} \chi_r \, d\chi_r}{\int p(\chi_r, \varepsilon_r) \, d\chi_r}, \tag{4.7}$$

which gives (see Appendix A)

$$\langle (C_\theta^2)_r | \varepsilon_r \rangle = \gamma \bar{\chi}_r \varepsilon_r^{-1/3} \exp \left[\frac{1 - \rho_{xy}^2 \sigma_y^2}{2 \sigma_y^2} \right] \left(\frac{\varepsilon_r}{\bar{\varepsilon}_r} \right)^{\rho_{xy} \sigma_y / \sigma_x}. \tag{4.8}$$

That is, we have the power law

$$\langle (C_\theta^2)_r | \varepsilon_r \rangle \propto \varepsilon_r^\delta \tag{4.9}$$

with the exponent, or ‘logarithmic slope’,

$$\delta = \rho_{xy} \frac{\sigma_y}{\sigma_x} - \frac{1}{3}. \tag{4.10}$$

As described in §3, the primary observables obtained with the inertial-range technique are ε_r and $(C_\theta^2)_r$. Therefore, it is more natural to express $\langle (C_\theta^2)_r | \varepsilon_r \rangle$ in terms of $(C_\theta^2)_r$ and ε_r statistics, rather than in terms of χ_r and ε_r statistics. In logarithmic notation, the Obukhov–Corrsin relation is $z = -x/3 + y$, where

$$z = \ln \frac{(C_\theta^2)_r}{\overline{(C_\theta^2)_r}} \tag{4.11}$$

is the logarithm of the normalized temperature structure parameter, where $\overline{(C_\theta^2)_r}$ is chosen such that $\langle z \rangle = 0$, and where σ_z is the standard deviation of z . It is known that x and $z = ax + by$ (with real numbers a and b) are jointly normal if x and y are jointly normal (e.g. Davenport & Root 1958, p. 151). Therefore, $(C_\theta^2)_r$ and ε_r are jointly lognormal if χ_r and ε_r are jointly lognormal. Based on the same dataset that we will analyse in the following, Frehlich *et al.* (2004) have shown that joint lognormality for $(C_\theta^2)_r$ and ε_r is a good approximation in the shear region of the nocturnal low-level jet.

With (A 14), we obtain

$$\langle (C_\theta^2)_r | \varepsilon_r \rangle = \overline{(C_\theta^2)_r} \exp \left[\frac{1 - \rho_{xz}^2 \sigma_z^2}{2 \sigma_z^2} \right] \left(\frac{\varepsilon_r}{\bar{\varepsilon}_r} \right)^{\rho_{xz} \sigma_z / \sigma_x}, \tag{4.12}$$

where ρ_{xz} is the correlation coefficient of the logarithms of $(C_\theta^2)_r$ and ε_r . Therefore, the slope in terms of inertial-range measurables is

$$\delta = \rho_{xz} \frac{\sigma_z}{\sigma_x}. \tag{4.13}$$

From (2.4) and (2.5) we find that

$$\frac{\sigma_y}{\sigma_x} = \sqrt{\frac{A_\theta + \mu_\theta \ln(L_\theta/r)}{A + \mu \ln(L/r)}}. \tag{4.14}$$

For $r \ll L$ and $r \ll L_\theta$, the ratio σ_y/σ_x approaches the asymptotic value $\sqrt{\mu_\theta/\mu}$. Antonia & Van Atta (1975) hypothesized that $\mu_\theta \approx \mu$. In that case, $\sigma_y/\sigma_x \approx 1$, and

because the correlation coefficient ρ_{xy} cannot exceed 1, δ cannot exceed the value $2/3$. This argument, however, is valid only if r is ‘deep in the inertial range’, such that $r/L \ll 1$. Also, one has to keep in mind that the ratios L_θ/r and L/r enter only logarithmically in the expression for σ_y/σ_x , such that unrealistically large values for L_θ/r and L/r may have to be assumed to infer that σ_y/σ_x is close to one. Therefore, the result that δ cannot exceed the value $2/3$ has to be taken with caution, particularly since little is known about the magnitude of the coefficients A and A_θ .

Antonia & Van Atta (1975, p. 280) argued that in order to be consistent with the $r^{2/3}$ dependence of the second-order scalar structure function (i.e. of $\langle(\Delta\theta)^2\rangle$), ρ_{xy} is required to be equal to $2/3$. With the additional assumption $\sigma_x = \sigma_y$, this leads to a power-law exponent $\delta = 1/3$. We will return to these issues when we discuss the results from the fine-wire measurements.

4.2. The large-scale intermittency model

In micrometeorology, it is a traditional working assumption that estimates of low-order turbulence statistics like variances and structure parameters are statistically stable if the length of the time series from which the statistics are estimated is at least 10 min or so. The underlying assumption is that there is a sufficiently clear scale separation between small-scale turbulence and large-scale turbulence. This scale separation is also known as the ‘mesoscale gap’ or ‘spectral gap’ (Van der Hoven 1957); see also Lumley & Panofsky (1964, pp. 42ff.), Fiedler & Panofsky (1970), and Mahrt, Moore & Vickers (2001). Recently, Vickers & Mahrt (2003) have described a ‘co-spectral gap,’ which they found in spectra of turbulent fluxes measured during CASES-99.

Let us denote with σ_u^2 and σ_θ^2 the variances of streamwise velocity and temperature, respectively, associated with three-dimensional turbulence. Let us assume that the structure functions $D_{11}(s)$ and $D_{\theta\theta}(s)$ follow the inertial-range laws (3.8) and (3.9) for separations s up to some outer scales L_u and L_θ , respectively, and that for larger separations the structure functions approach the constant values $2\sigma_u^2$ and $2\sigma_\theta^2$, respectively. It is natural to define L_u and L_θ as the separations at which the inertial-range asymptotes and the constant asymptotes intersect, such that

$$C_u^2 L_u^{2/3} = 2\sigma_u^2 \quad (4.15)$$

and

$$C_\theta^2 L_\theta^{2/3} = 2\sigma_\theta^2. \quad (4.16)$$

Now, we follow Prandtl (1925) and define a velocity *mischungsweglänge*, or velocity mixing length, l_u and a scalar mixing length l_θ such that the magnitude of the systematic change across the mixing length is equal to the standard deviation associated with the turbulent fluctuations:

$$\left| \frac{\partial U}{\partial z} \right| l_u = \sigma_u \quad (4.17)$$

and

$$\left| \frac{\partial \Theta}{\partial z} \right| l_\theta = \sigma_\theta. \quad (4.18)$$

Here, $\partial U/\partial z$ and $\partial \Theta/\partial z$ are the vertical gradients of mean velocity and the mean potential temperature, respectively.

After combining these last four equations and eliminating σ_u and σ_θ , we obtain a relationship between C_u^2 and C_θ^2 :

$$C_\theta^2 = \frac{L_u^{2/3} l_\theta^2 (\partial\Theta/\partial z)^2}{L_\theta^{2/3} l_u^2 (\partial U/\partial z)^2} C_u^2, \tag{4.19}$$

or

$$C_\theta^2 = C_K ab \varepsilon^{2/3}, \tag{4.20}$$

where

$$a \equiv \frac{L_u^{2/3} l_\theta^2}{L_\theta^{2/3} l_u^2} \tag{4.21}$$

and

$$b \equiv \frac{(\frac{\partial\Theta}{\partial z})^2}{(\frac{\partial U}{\partial z})^2} \tag{4.22}$$

are parameters that are allowed to vary randomly as a result of large-scale intermittency, and where $C_K = 2.0$ is the coefficient in (3.16).

Here, we consider two special cases: first, the parameter

$$q \equiv C_K ab = \frac{L_u^{2/3} l_\theta^2 (\partial\Theta/\partial z)^2}{L_\theta^{2/3} l_u^2 (\partial U/\partial z)^2} \tag{4.23}$$

is statistically independent of ε ; second, shear and stratification are coupled through the Richardson criterion.

If q is statistically independent of ε , we have $p_{q\varepsilon}(q, \varepsilon) = p_q(q)p_\varepsilon(\varepsilon)$, where $p_{q\varepsilon}(q, \varepsilon)$ is the j.p.d.f. of q and ε , $p_q(q)$ is the p.d.f. of q , and $p_\varepsilon(\varepsilon)$ is the p.d.f. of ε . Therefore,

$$\langle C_\theta^2 | \varepsilon \rangle \equiv \frac{\int p_{q\varepsilon}(q, \varepsilon) C_\theta^2(q, \varepsilon) dq}{\int p_{q\varepsilon}(q, \varepsilon) dq} = \frac{\int p_q(q) p_\varepsilon(\varepsilon) q \varepsilon^{2/3} dq}{\int p_q(q) p_\varepsilon(\varepsilon) dq}, \tag{4.24}$$

and we obtain immediately

$$\langle C_\theta^2 | \varepsilon \rangle = \langle q \rangle \varepsilon^{2/3}. \tag{4.25}$$

That is, the slope is $\delta = 2/3$ if q is statistically independent of ε .

In the second scenario, we assume that the turbulence is in ‘Richardson equilibrium’ everywhere in the space–time window under consideration. That is, the statistical ensemble is assumed to contain only combinations of mean shear $\partial U/\partial z$ and mean stratification $\partial\Theta/\partial z$ that satisfy the Richardson criterion

$$Ri_c = \frac{g}{\Theta} \frac{\partial\Theta/\partial z}{(\partial U/\partial z)^2}. \tag{4.26}$$

Here, Ri_c is a critical Richardson number, which we assume to have a universal value close to its traditional value $1/4$, g is acceleration due to gravity, and Θ is the mean potential temperature at the altitude of interest.

Solving (4.26) for $(\partial U/\partial z)^2$ and inserting into (4.19) leads to

$$C_\theta^2 = a Ri_c \frac{\Theta}{g} \frac{\partial\Theta}{\partial z} C_u^2 \tag{4.27}$$

or

$$C_\theta^2 = a Ri_c C_K \frac{\Theta^2}{g^2} N^2 \varepsilon^{2/3}, \quad (4.28)$$

where

$$N = \sqrt{\frac{g}{\Theta} \frac{\partial \Theta}{\partial z}} \quad (4.29)$$

is the Brunt–Väisälä frequency.

The coefficients C_K and Ri_c and the parameter g/Θ may be considered as constants. Furthermore, let us follow conventional wisdom and assume that all four length scales are of order L , such that a may also be treated as a quasi-universal coefficient. Then the coefficient $a Ri_c C_K$ is also a constant of order unity. If N is statistically independent of ε , which is the case if fluctuations in ε result from changes in shear, rather than from changes in thermal stability, we find

$$\langle C_\theta^2 | \varepsilon \rangle = a Ri_c C_K \frac{\Theta^2}{g^2} \langle N^2 \rangle \varepsilon^{2/3}. \quad (4.30)$$

That is, the large-scale intermittency model predicts an $\varepsilon^{2/3}$ law for $\langle C_\theta^2 | \varepsilon \rangle$, regardless of whether (i) shear and stratification are statistically independent, or (ii) shear and stratification ‘track’ each other because they are deterministically connected through the Richardson criterion.

5. Experimental setup and meteorological situation

5.1. CIRES tethered lifting system (TLS) and turbulence sensors

The observations reported here were obtained from high-resolution *in-situ* turbulence observations in the lowest few hundred metres of the night-time atmosphere approximately 40 km east of Wichita, Kansas, during the Cooperative Atmosphere-Surface Exchange Study (CASES-99). CASES-99 was designed to study the structure and dynamics of the night-time stable boundary layer (Poulos *et al.* 2002). *In situ* data were recorded using the Cooperative Institute for Research in Environmental Sciences (CIRES) Tethered Lifting System (TLS), which employs either a kite or an aerodynamic balloon (kites for moderate-to-strong wind conditions; balloons for low wind conditions) to carry a suite of lightweight instruments from the ground up through the first few kilometres of the atmosphere (Balsley, Jensen & Frehlich 1998; Muschinski *et al.* 2001; Balsley *et al.* 2003; Frehlich *et al.* 2003).

For CASES-99, the TLS instrumentation included up to five ‘turbulence payloads’ (TPs) separated vertically by pre-selected spacings. The TPs could be attached above or below the basic meteorological payload (BMP). The measurements collected with the TPs were calibrated and converted into accurate turbulence data only after the field campaign. The BMP consisted of a Vaisala RS-80 radiosonde and a Tmax-board interface, and its main purpose was to provide real-time data of pressure, wind speed and direction, and temperature, thereby enabling scientists and technicians on the ground to respond to the ever-changing structure and dynamics of the NBL and to move the TPs up and down as required. None of the data collected with the BMP were used for the calibration of the temperature and velocity data measured with the TPs. After the field campaign, the turbulence data obtained from each of the five TPs were calibrated independently from the BMP and independently from each other. The pressure data from the BMP were used to reconstruct the time series of the altitudes of each TP.

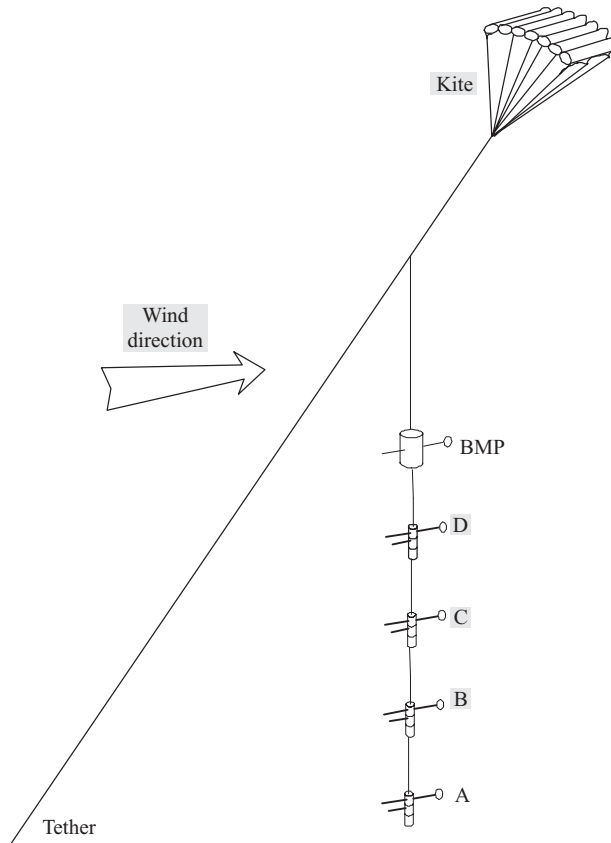


FIGURE 1. Sketch of the CIRES Tethered Lifting System (TLS), carrying a vertical array of four turbulence sensors (A, B, C, and D) and the basic meteorological payload (BMP) up to altitudes of 500 m above ground level (AGL).

Each TP archived data measured with both cold-wire and hot-wire sensors. The cold- and hot-wire data were sampled at 200 Hz. Each TP also carried conventional low-frequency sensors (e.g. a Pitot tube, a solid-state temperature sensor, and a piezoelectric pressure sensor) for sampling wind speed, temperature, and pressure, along with a 3-axis tilt sensor and a magnetic compass. Separate archiving for each TP was accomplished using onboard digital flash-memory storage, with data downloads to disk occurring when the packages were brought down to the ground at the end of each night of operation. Figure 1 is a sketch of the TLS and the sensor-array in the configuration of the CASES-99 deployment during the night of 20/21 October 1999. During that night, the TLS was operated with a kite, and the sensor array consisted of the four TPs A, B, C, and D (from bottom to top), and the BMP. The vertical spacing between the turbulence payloads was 6 m.

The last step of the calibration procedure was to ‘merge’ the low- and high-frequency data measured with each TP into 200 Hz time series of temperature and streamwise velocity. This procedure and the specifications of the individual sensors are described in detail in Frehlich *et al.* (2003). The merged time series inherit the high long-term stability of the low-frequency sensors and the excellent sensitivity and short response times of the fine-wire sensors. The absolute accuracy of the merged temperature

and velocity data is better than 0.5 K and 1 m s^{-1} , respectively. The cold and hot wires were operated with low-pass filters with 3 dB cutoff frequencies of 500 Hz and 2 kHz, respectively. Although no anti-aliasing filter was used, the uncorrelated noise standard deviations in the temperature and velocity samples were as small as 1 mK and 1.7 mm s^{-1} , respectively. These estimates were obtained from the spectra shown in figures 8 and 9 in Frehlich *et al.* (2003).

Consecutive one-second periods of temperature and streamwise velocity fluctuations sampled at 200 Hz were spectrally analysed to produce estimates of $(C_\theta^2)_r$ and ε_r , respectively, by means of the inertial-range technique described in §3. The sampling uncertainty of these 1 s estimates is better than 15%, which implies a 15% accuracy for $(C_\theta^2)_r$ and 22.5% accuracy for ε_r ; see Frehlich *et al.* (2003) for further details.

As described in §3, the local Taylor hypothesis was used. Because the averaging time τ is related to the averaging length r via $r = U_r \tau$, a fixed averaging time ($\tau = 1\text{ s}$) leads to a changing r if the wind speed changes. Because in the data set U_r ranged between about 5 m s^{-1} and 13 m s^{-1} , r varied between 5 m and 13 m. The variances σ_x^2 and σ_z^2 are expected to increase with decreasing r , such that the sections with low wind speeds should reveal larger values of σ_x^2 and σ_z^2 than the sections with higher wind speeds. However, since σ_x^2 and σ_y^2 are expected to vary only with the logarithm of r , we neglect this effect.

5.2. Meteorological situation

Figure 2 shows three vertical profiles of wind speed and temperature, respectively, observed with the TLS during three ascents. The first ascent (20:58 LST to 21:12 LST) reached an altitude of 340 m, the second (22:40 LST to 23:04 LST) reached 330 m, and the third ascent (01:10 LST to 01:31 LST) reached 450 m. All data points shown here are averages over 1 min. That is, a typical ascent rate was 20 m min^{-1} , or about 0.3 m s^{-1} .

The dynamics in the lowest 200 m AGL were dominated by a low-level jet with a wind speed maximum between 12 m s^{-1} and 14 m s^{-1} at altitudes around 150 m (figure 2a). After midnight, the intensity of the jet as well as the magnitudes of the shear both below and above the jet decreased significantly, which led to a drastic reduction of turbulence production in the upper part of the NBL. As a result, a very sharp inversion at about 190 m was formed. This inversion marked the top of the NBL. As documented by Balsley *et al.* (2003), the thickness of this inversion was as small as 5 cm. The temperature change across these 5 cm was about 2 K.

As can be seen in figure 2(b), the thermal stratification in the NBL was rather strong, with $\partial\theta/\partial z \approx 0.05\text{ K m}^{-1}$, which is five times as much as in an isothermal atmosphere. During the second ascent, the shear in the lowest 100 m was 0.10 s^{-1} and the potential temperature gradient was 0.04 K m^{-1} , resulting in a gradient Richardson number of 0.13 below the jet, about half the traditional value of the critical Richardson number, 0.25. That is, the NBL below the jet was dynamically unstable and turbulent, also later in the night, which is evident from the fairly intense turbulence, as will be documented in the following. During the night, the NBL cooled down with typical rates of 1 K h^{-1} .

In the residual layer above the NBL top, thermal stratification and wind shear were much less than in the NBL. Gradient Richardson numbers (estimated from altitude intervals of 20 m or so) in the residual layer were typically much larger than 0.25.

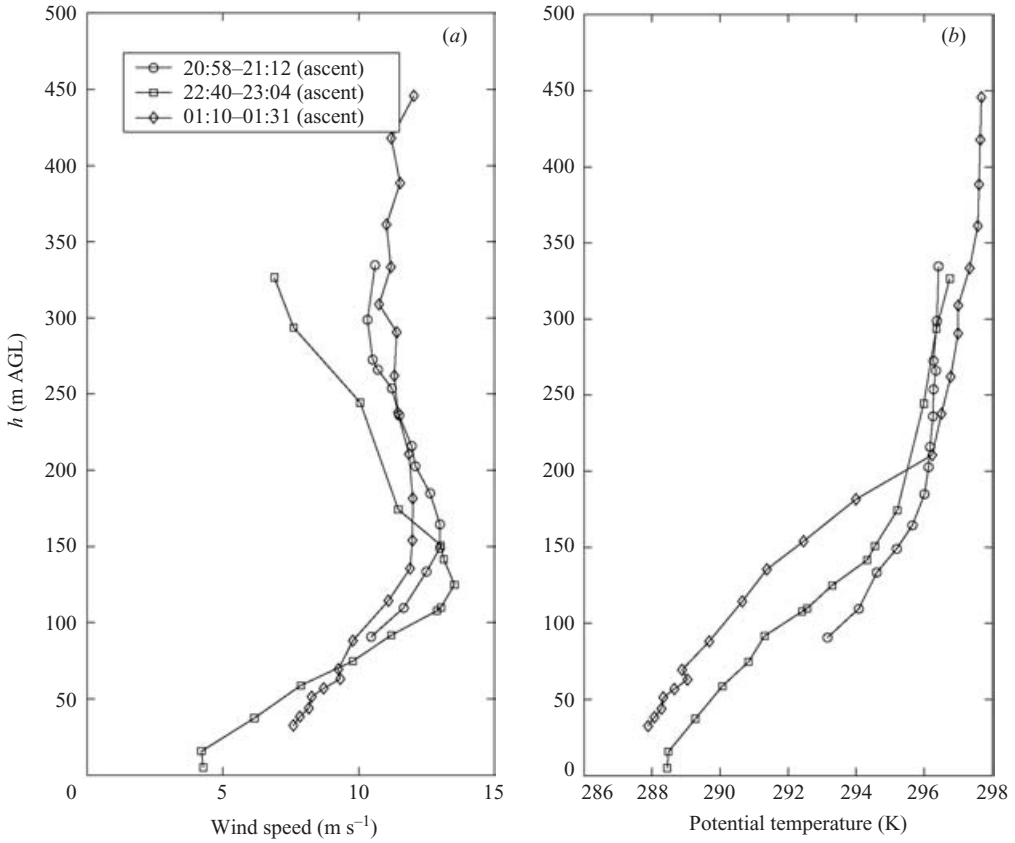


FIGURE 2. Vertical profiles of 1 min averages of (a) the wind speed and (b) the potential temperature. Data were taken with sensor C during three different ascents. The wind speed maximum associated with the low-level jet was at about 150 m AGL. The top of the nocturnal boundary layer (NBL) was between 150 and 200 m AGL. Thermal stratification (b) was strongly stable in the NBL and weakly stable in the overlying residual layer.

6. Observations

6.1. Time series

Figure 3 gives an overview of the measurements taken with sensor C during the night of 20/21 October 1999. Ten-hour time series of 1 s estimates of the following quantities are shown: (a) the sensor altitude h above ground level; (b) the wind speed u ; (c) the air temperature T ; (d) the local energy dissipation rate ε_r ; and (e) the local temperature variance dissipation rate χ_r . In figure 3(a), three episodes are marked: NBL, for ‘nocturnal boundary layer’, between 03:00 and 05:00 LST at altitudes between 52 m and 74 m AGL; RL, for ‘residual layer’, between 21:20 and 22:20 LST at altitudes between 167 m and 224 m AGL; and AD, for ‘ascent/descent’, between 01:10 and 01:50 LST at altitudes between 32 m and 452 m AGL. The NBL and RL episodes were chosen because the sensors were ‘parked’ at roughly constant height during those episodes, and the observed fluctuations were nearly statistically stationary. The AD episode consists of two vertical soundings of the nocturnal boundary layer and the lower residual layer.

Time series measured during the episodes NBL, RL, and AD are shown in more detail in figures 4, 5, and 6, respectively.

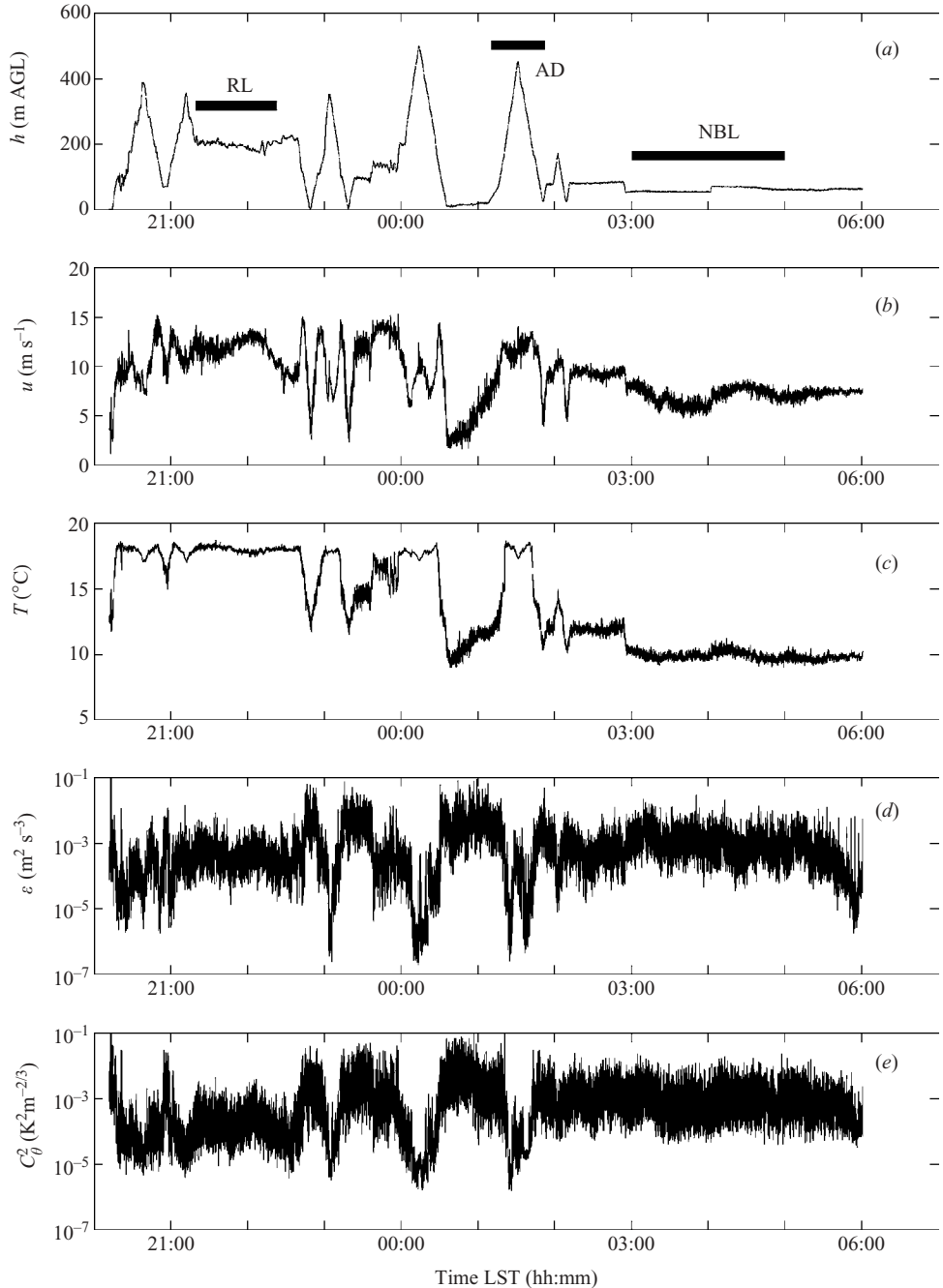


FIGURE 3. Overview of the turbulence measurements collected with sensor package C during the night of 20/21 October 1999. (a) Sensor altitude above ground level (AGL); (b) wind speed (1 s averages); (c) air temperature (1 s averages); (d) local energy dissipation rate, ε_r , estimated from 1 s time series of wind speed fluctuations sampled at 200 Hz; (e) local temperature structure parameter, $(C_\theta^2)_r$, estimated from 1 s time series of temperature fluctuations sampled at 200 Hz. Detailed time series measured during the episodes annotated in (a) as NBL (for 'nocturnal boundary layer', from 03:00 LST to 05:00 LST), as RL (for 'residual layer', from 21:20 LST to 22:20 LST), and as AD (for 'ascent/descent', from 01:10 LST to 01:50 LST) are shown in figures 4(a-e), 5(a-e), and 6(a-e), respectively.

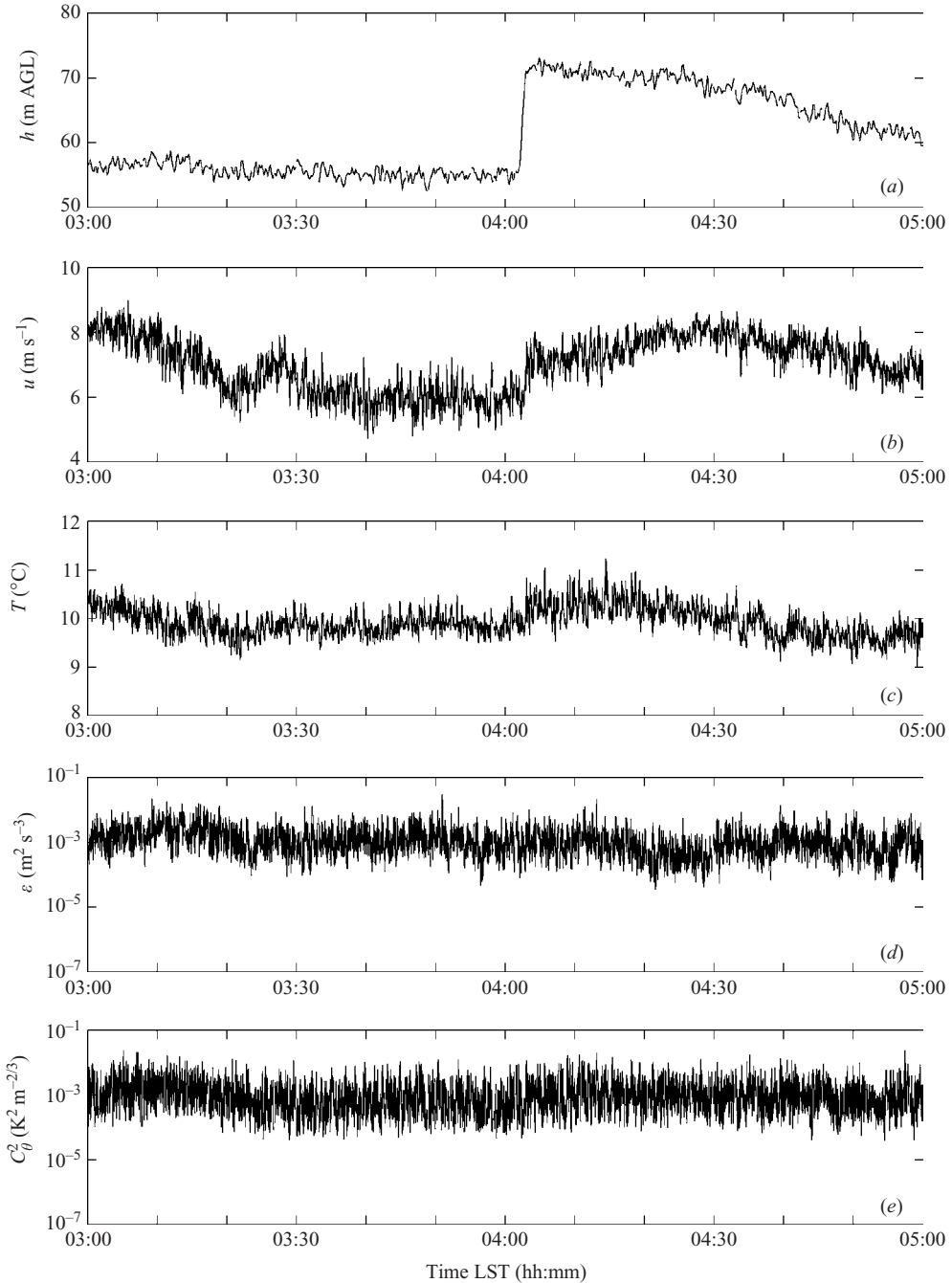


FIGURE 4. Same as figure 3(a-e) but for the NBL (nocturnal boundary layer) episode between 03:00 LST and 05:00 LST.

6.2. Velocity and temperature spectra

Frequency spectra $S_{uu}(f)$ and $S_{\theta\theta}(f)$ of wind speed and temperature fluctuations measured during the NBL episode are shown in figure 7(a). Both $S_{uu}(f)$ and $S_{\theta\theta}(f)$ show two regimes in which the spectral densities vary with $f^{-5/3}$. Both in $S_{uu}(f)$ and

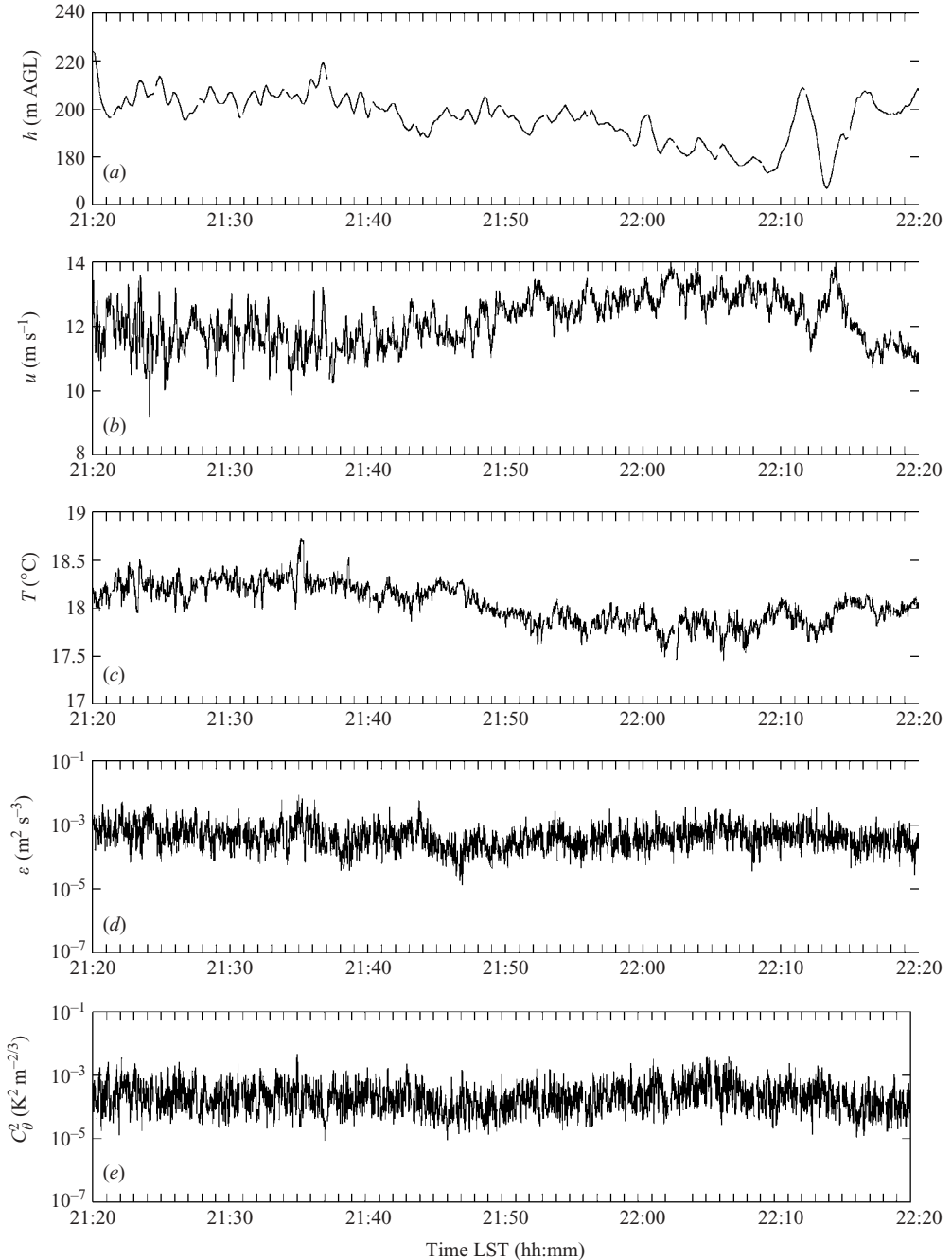


FIGURE 5. Same as figure 3 (*a–e*) but for the RL (residual layer) episode between 21:20 LST and 22:20 LST.

$S_{\theta\theta}(f)$, the two $f^{-5/3}$ regimes are separated by a plateau. Figure 7(*b*) shows the same data as in figure 7(*a*) but in ‘area-preserving’ representation. That is, figure 7(*b*) shows $fS_{uu}(f)$ and $fS_{\theta\theta}(f)$ in a semilogarithmic diagram.

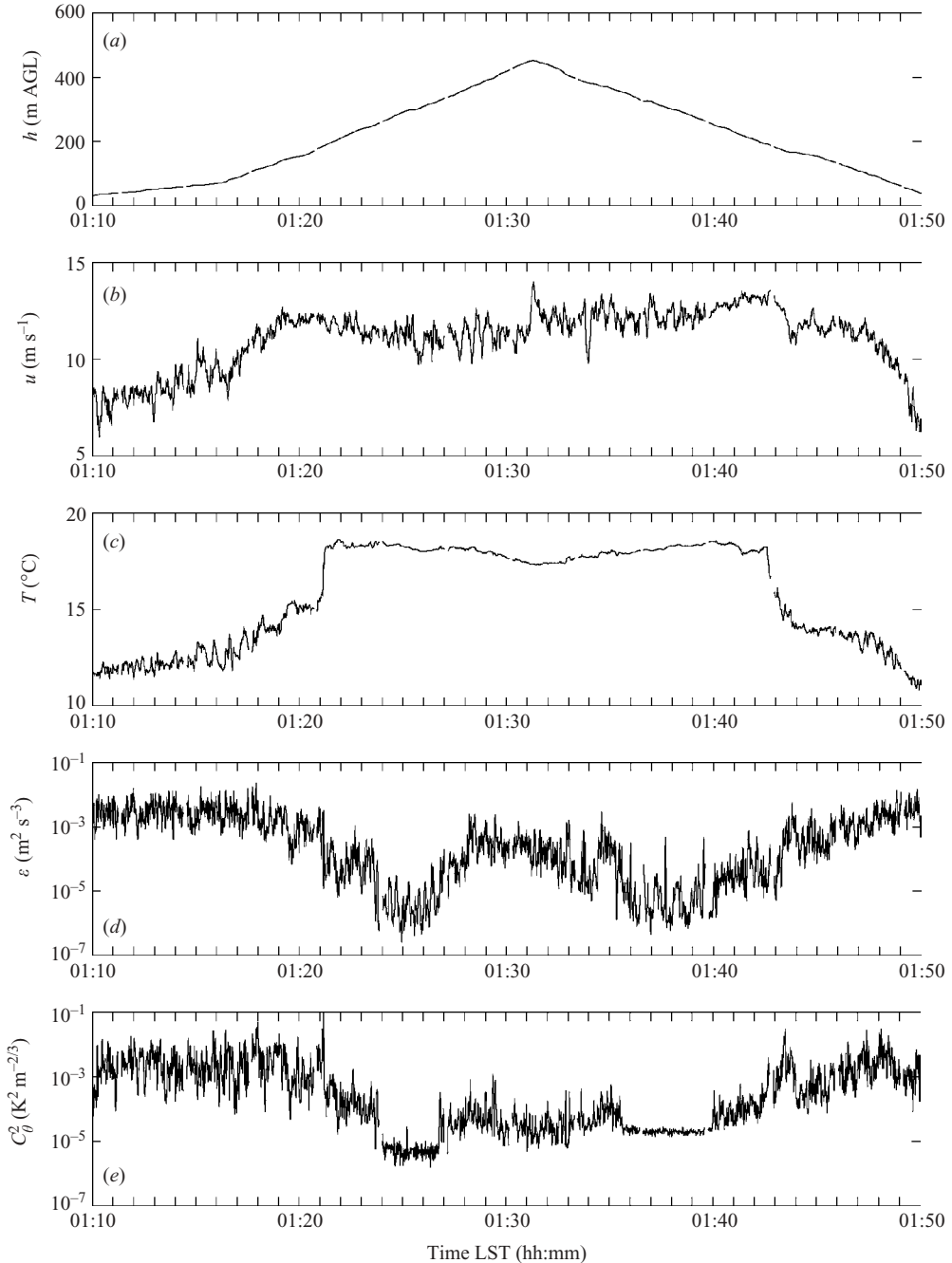


FIGURE 6. Same as figure 3 (*a–e*) but for the AD (ascent/descent) episode between 01:10 LST and 01:50 LST.

In both $S_{uu}(f)$ and $S_{\theta\theta}(f)$, the plateau ranges from 0.003 Hz (5.5 min) to 0.03 Hz (0.5 min), corresponding to wavelengths between 230 m and 2.3 km. Note that the frequencies of the minima and maxima in the area-preserving spectra shown

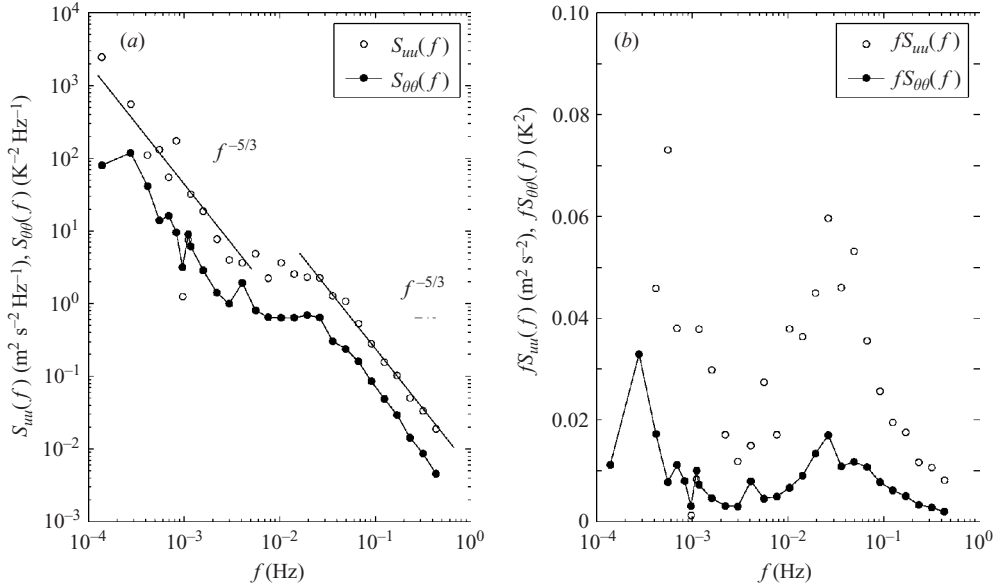


FIGURE 7. (a) Frequency spectra of wind speed and temperature fluctuations in double-logarithmic representation. The data were collected during the NBL episode (from 03:00 LST to 05:00 LST). Two regimes showing a $-5/3$ power law are separated by a plateau between 0.005 Hz and 0.02 Hz, corresponding to time scales ranging from 50 s to 3.3 min and (at a mean wind speed of $U = 7 \text{ m s}^{-1}$) to length scales between 350 m and 1400 m. (b) Same data as in (a) but in ‘area-preserving’ representation. The high-frequency and low-frequency boundaries of the plateau in (a) coincide with the spectral peak and the spectral gap, respectively, in (b).

in figure 7(b) coincide with the frequencies at the lower and upper, respectively, boundaries of the plateaux in figure 7(a), as expected.

The wavelength corresponding to the high-frequency end of the plateau marks the large-scale boundary of the inertial subrange of the three-dimensional, Kolmogorov-type turbulence. Muschinski & Roth (1993) argued that at an altitude h the largest features that could be statistically isotropic in three dimensions cannot have a radius larger than h , or a diameter larger than $2h$, or a wavelength larger than

$$\lambda_m = 4h. \quad (6.1)$$

The data presented in figure 7 were taken at altitudes around 65 m AGL. This leads to $\lambda_m = 260 \text{ m}$ and agrees well with the observed wavelength of 230 m. More discussion on this issue is given in § 7.1.

6.3. Scatter diagrams of ε_r and $(C_\theta^2)_r$; conditional averages of $(C_\theta^2)_r$ for specified values of ε_r

The local energy dissipation rates, ε_r , and local temperature structure parameters, $(C_\theta^2)_r$, which were shown as time series in figures 3–6, are presented in the form of scatter diagrams in figures 8(a), 9(a), 10(a), and 11(a), respectively. Figures 8(b), 9(b), 10(b), and 11(b) show, for the respective ensemble (the entire night, NBL, RL, or AD), conditional averages $\langle (C_\theta^2)_r | \varepsilon_r \rangle$ as functions of ε_r . The dots are linear averages of $(C_\theta^2)_r$ computed for specific ε_r bins, each of which has a width of $1/20$ decade. The lines are

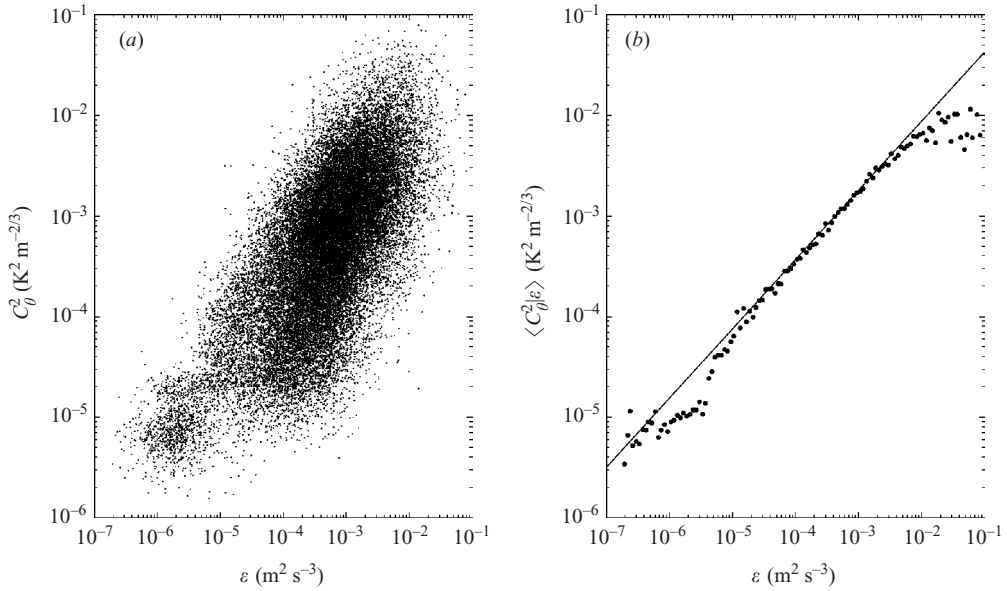


FIGURE 8. (a) Scatter diagram of all $(C_\theta^2)_r$ and ϵ_r values measured with sensor C during the night of 20/21 October 1999. The plot contains 33 660 data points. Statistical parameters: $\sigma_x = 1.86$, $\sigma_z = 1.82$, $\rho_{xz} = 0.70$. (b) Conditional averages of $(C_\theta^2)_r$ for specified values of ϵ_r . The width of the ϵ_r bins is 1/20 decade. The solid line is the model resulting from (4.12), which assumes joint lognormality of $(C_\theta^2)_r$ and ϵ_r . The slope predicted from (4.12) is $\delta = \rho_{xz}\sigma_z/\sigma_x = 0.69$.

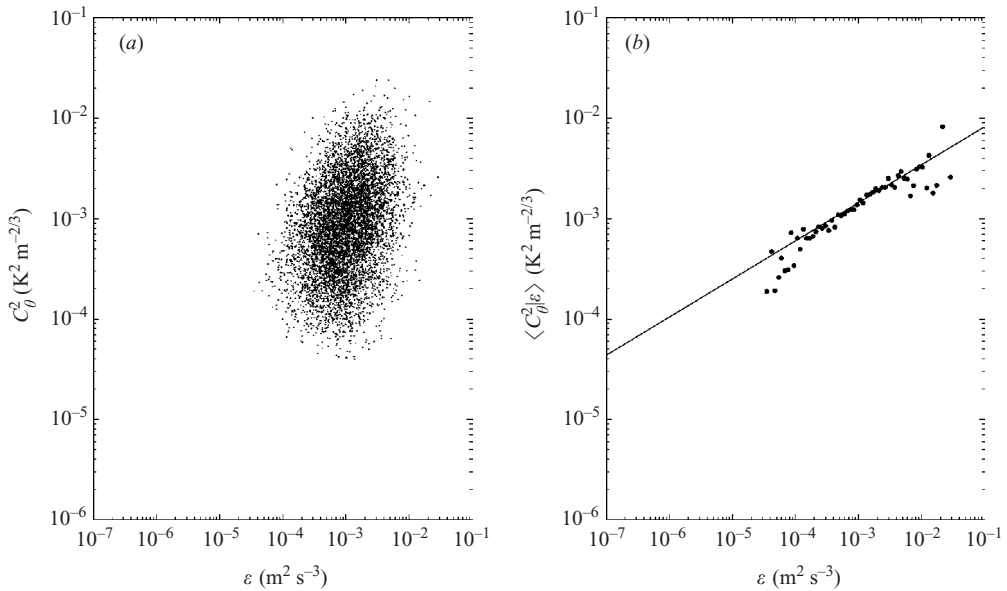


FIGURE 9. Same as figure 8(a,b) but for the NBL (nocturnal boundary layer) episode between 03:00 LST and 05:00 LST. The scatter diagram (a) contains 6859 data points. Statistical parameters: $\sigma_x = 0.93$, $\sigma_z = 1.09$, $\rho_{xz} = 0.32$. The slope predicted from (4.12) is $\delta = 0.38$.

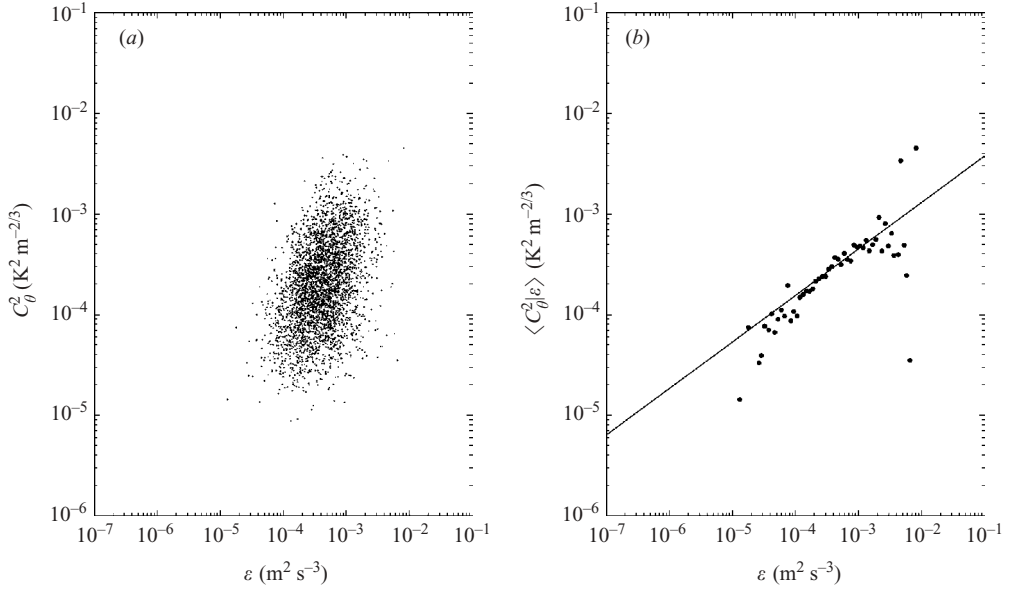


FIGURE 10. Same as figure 8(a, b) but for the RL (residual layer) episode between 21:20 LST and 22:20 LST. The scatter diagram (a) contains 3430 data points. Statistical parameters: $\sigma_x = 0.83$, $\sigma_z = 1.01$, $\rho_{xz} = 0.38$. The slope predicted from (4.12) is $\delta = 0.46$.

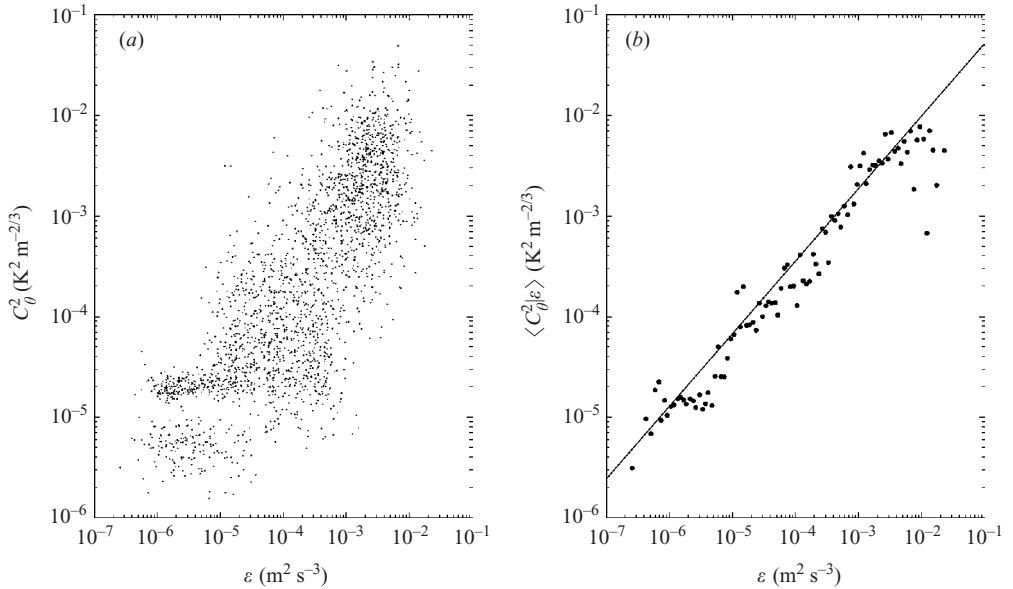


FIGURE 11. Same as figure 8(a, b) but for the AD (ascent/descent) episode between 01:10 LST and 01:50 LST. The scatter diagram (a) contains 2284 data points. Statistical parameters: $\sigma_x = 2.51$, $\sigma_z = 2.29$, $\rho_{xz} = 0.80$. The slope predicted from (4.12) is $\delta = 0.72$.

the theoretical power laws obtained from (4.12) with the respective values of $\overline{(C_\theta^2)_r}$, $\overline{\epsilon_r}$, σ_x , σ_z , and ρ_{xz} . Table 1 gives an overview of the statistical parameters characterizing the four ensembles. Relationships between these statistical parameters are derived in Appendix B.

	$\overline{(C_\theta^2)_r}$ [K ² m ^{-2/3}]	$\overline{\varepsilon_r}$ [m ² s ⁻³]	σ_x	σ_z	ρ_{xz}	σ_y	ρ_{xy}	σ_y/σ_x	δ
all	4.3×10^{-4}	4.3×10^{-4}	1.86	1.82	0.70	2.30	0.83	1.24	0.69
NBL	8.3×10^{-4}	9.7×10^{-4}	0.93	1.09	0.32	1.23	0.54	1.32	0.38
RL	1.9×10^{-4}	4.0×10^{-4}	0.83	1.01	0.38	1.14	0.58	1.37	0.46
AD	2.1×10^{-4}	1.8×10^{-4}	2.51	2.29	0.80	3.00	0.89	1.19	0.72

TABLE 1. Statistical parameters characterizing the four data ensembles ‘all’ (20:12 LST to 06:01 LST), NBL (03:00 to 05:00 LST), RL (21:20 to 22:20 LST), and AD (01:10 to 01:50 LST).

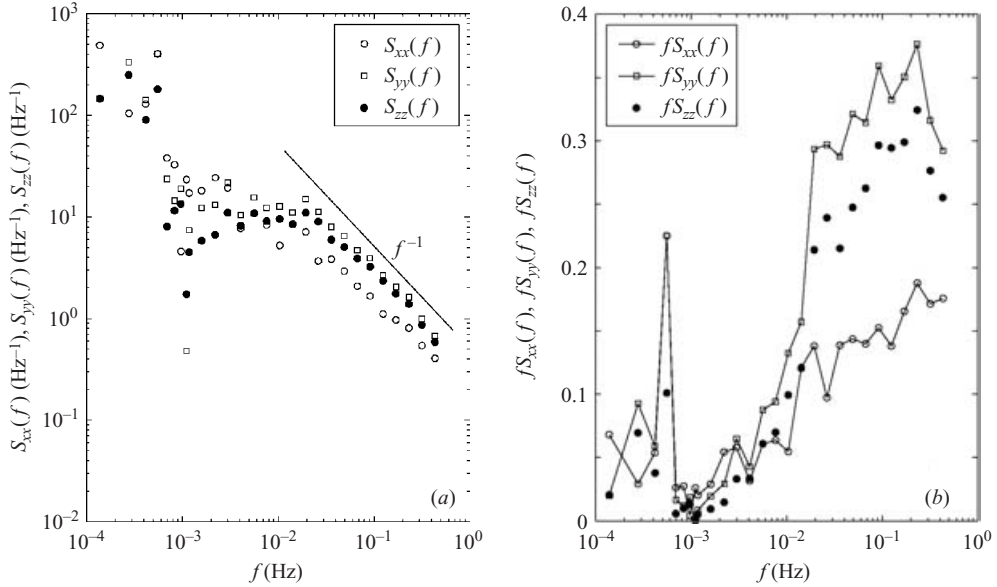


FIGURE 12. Same as figure 7 but showing spectra of x (the logarithm of ε_r), y (the logarithm of χ_r , calculated from ε_r and $(C_\theta^2)_r$ through the Obukhov–Corrsin relation), and z (the logarithm of $(C_\theta^2)_r$). As in figure 7, data were collected during the NBL episode. At high frequencies, the spectra of x , y , and z show a f^{-1} power law, in agreement with Kolmogorov’s (1962) lognormality hypothesis.

6.4. Spectra of the logarithms of ε_r , χ_r , and $(C_\theta^2)_r$

Figures 12 and 13 show frequency spectra of x , y , and z (i.e. of the centralized logarithms of ε_r , χ_r , and $(C_\theta^2)_r$) observed during the NBL and RL episodes, respectively. At frequencies higher than about 0.03 Hz (wavelengths shorter than 230 m), all spectra follow (approximately) an f^{-1} power law.

7. Discussion

7.1. Three-dimensional and quasi-two-dimensional regimes in stratified shear flow

The velocity and temperature spectra in figure 7 show $f^{-5/3}$ regimes at frequencies lower than 0.003 Hz (wavelengths longer than 2.3 km) and at frequencies higher than 0.03 Hz (wavelengths shorter than 230 m). These two $-5/3$ regimes are separated by a plateau.

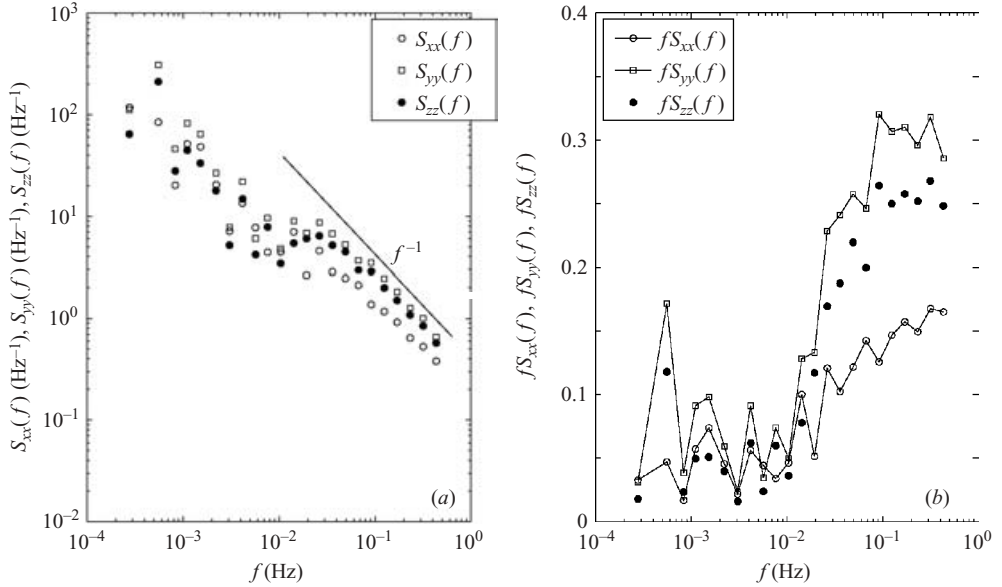


FIGURE 13. Same as figure 12 but for the RL episode.

The $-5/3$ power-law behaviour at small scales is expected from classical inertial-range theories for three-dimensionally isotropic velocity turbulence (Kolmogorov 1941; Obukhov 1941*a,b*) and three-dimensionally isotropic temperature turbulence (Obukhov 1949; Corrsin 1951). The observed wavelength of the largest eddies in that regime agrees well with the ‘isotropic cutoff’ wavelength $\lambda_m = 4h$ (h being the altitude above ground level) predicted by the simple Muschinski & Roth (1993) model. Of course, λ_m can be only a rough approximation of the wavelength that separates the isotropic from the anisotropic regime. In the real atmosphere, the transition from three-dimensional to two-dimensional flow occurs gradually. Although it may well be that the features with the horizontal wavelength λ_m were strongly squeezed in the vertical direction and therefore strongly anisotropic, we cannot quantify the degree of anisotropy based on our data. Regardless of the possible anisotropy, however, $\lambda_m = 4h$ appears to be a good approximation of the horizontal wavelength at which the streamwise spectra show the transition from the plateau to the $-5/3$ power law characterizing the small-scale turbulence.

The physics of the $-5/3$ power law at wavelengths longer than 2.3 km is less clear. The low-frequency parts of the spectra represent quasi-two-dimensional velocity and temperature fluctuations advected past the sensors by the horizontal wind. Spectra following a $-5/3$ power law in the quasi-two-dimensional wavenumber regime have previously been observed in the ocean (Ozmidov 1965) and in the atmosphere (e.g. Gage 1979; Nastrom & Gage 1985) but their physical nature is still a matter of debate.

Ozmidov (1965) suggested that in general there is a forward energy cascade, transferring energy from the largest scales to the smallest scales. According to his conceptual model, the spectral density varies like $k_1^{-5/3}$ (k_1 being the wavenumber in the streamwise direction) except within wavenumber bands of intensified energy supply, where spectral ‘bumps’ and plateaux occur. Ozmidov (1965) identified three sources of energy supply for oceanic motion: major atmospheric disturbances, inertial

and tidal oscillations, and wind waves. In our case, gravity-wave breaking and Kelvin–Helmholtz (KH) instability are two mechanisms through which kinetic energy from the horizontal flow could be converted into three-dimensional turbulent kinetic energy. The wavelength of the fastest growing KH billows is about 7.5 times the thickness D of the shear layer (e.g. Fritts & Rastogi 1985). If D is of order 100 m, then the length of the dominating KH billows is of order 750 m. The horizontal wavelength of the dominating gravity waves is $2\pi U/N$, where $2\pi/N$ is the Brunt–Väisälä period, which in the NBL is about 1 min, which leads to a wavelength of 600 m for a wind speed of 10 m s^{-1} . Both wavelengths are between 230 m and 2.3 km, i.e. within the spectral plateau.

The idea that the energy generally cascades all the way down from the very large scales to the dissipation scales is inconsistent with two-dimensional turbulence theory (Kraichnan 1967), which requires an inverse cascade. A forward cascade, however, is consistent with the theory of gravity-wave breaking. Lilly (1983) investigated the ratio of the forward and inverse energy transfer rates and concluded that “the upscale escape of only a few percent of the total energy released by small-scale turbulence is apparently sufficient to explain the observed mesoscale energy spectrum of the troposphere”. Recently, Cho & Lindborg (2001) and Lindborg & Cho (2001) analysed aircraft measurements collected in the upper troposphere and lower stratosphere and found evidence that in the quasi-two-dimensional, mesoscale regime between 10 km and 100 km the energy is cascaded to smaller scales, not to larger scales as predicted by two-dimensional turbulence theory. Also the recent quasi-geostrophic two-level model simulations by Tung & Orlando (2003) support the notion of an energy source at very large scales but do not support the existence of an inverse cascade that would have to be fed by an energy source at small scales. The Tung & Orlando (2003) analysis, however, has to some extent been challenged by Smith (2004). See also the reply by Tung (2004).

Although we present no positive evidence for the forward cascade here, in our case a forward cascade appears to be a more natural explanation than the idea that the entire mesoscale spectrum would be generated and maintained by energy supply at scales of order 1 km.

7.2. Classical spectra and intermittency spectra

As shown in §6, our NBL observations of the ‘classical’ turbulence spectra $S_{uu}(f)$ and $S_{\theta\theta}(f)$ and of the ‘intermittency spectra’ $S_{xx}(f)$, $S_{yy}(f)$, and $S_{zz}(f)$ are all characterized by plateaux at intermediate frequencies and by power-law roll-offs at frequencies higher than 0.03 Hz, i.e. at wavelengths shorter than 230 m.

While the plateaux in the classical spectra separate small-scale turbulence from large-scale turbulence, the plateaux in the intermittency spectra may be seen as separating small-scale intermittency from large-scale intermittency. Small-scale intermittency is the random variability of the ‘turbulence parameters’ ε_r , χ_r , and $(C_\theta^2)_r$ in the three-dimensional regime, while large-scale intermittency is the random variability of ε_r , χ_r , and $(C_\theta^2)_r$ in the quasi-two-dimensional regime.

That the outer scale L is relevant for the small-scale intermittency statistics was hypothesized with great intuition by Kolmogorov (1962) and Obukhov (1962), and our observations support their view. However, Kolmogorov (1962) and Obukhov (1962) say nothing about large-scale intermittency. Figures 12 and 13 show clearly that on the low-frequency side of the plateaux, the spectral densities in the intermittency spectra increase with decreasing frequency, or with increasing length scales. Therefore, intermittency statistics like σ_x , σ_y , σ_z , ρ_{xy} , and ρ_{xz} vary with the sample size, implying

that any small-scale intermittency model is necessarily an incomplete description of atmospheric intermittency. The larger the sample, i.e. the wider the p.d.f.s of ε_r , χ_r , and $(C_\theta^2)_r$, the closer to 1 the correlation coefficients ρ_{xy} and ρ_{xz} become.

7.3. The f^{-1} law and the intermittency exponents

While, as expected from classical theory, $S_{uu}(f)$ and $S_{\theta\theta}(f)$ drop off like $f^{-5/3}$ at high frequencies, the intermittency spectra $S_{xx}(f)$, $S_{yy}(f)$, and $S_{zz}(f)$ decrease like f^{-1} . In the following, we offer a simple explanation for the f^{-1} law.

As described in §2.2, Kolmogorov (1962) and Obukhov (1962) hypothesized that the variance of the logarithm of the locally averaged energy dissipation rate, ε_r (where r is the linear dimension of the averaging volume) increases with decreasing r as

$$\sigma_x^2 = A + \mu \ln \frac{L}{r}. \quad (7.1)$$

Therefore, the increment $d\sigma_x^2$ is given by

$$d\sigma_x^2 = -\mu \frac{dr}{r}. \quad (7.2)$$

Since σ_x^2 may be written as an integral of the intermittency spectrum $S_{xx}(f)$, we have

$$d\sigma_x^2 = S_{xx}(f) df, \quad (7.3)$$

such that

$$S_{xx}(f) = -\frac{\mu}{r} \frac{dr}{df}. \quad (7.4)$$

With Taylor's hypothesis, $U = rf$, we obtain

$$S_{xx}(f) = \mu f^{-1} \quad (7.5)$$

and, correspondingly, for the scalar intermittency spectrum,

$$S_{yy}(f) = \mu_\theta f^{-1}. \quad (7.6)$$

That is, we have a theoretical explanation for the f^{-1} power law observed in the intermittency spectra, and the constants of proportionality turn out to be the intermittency exponents μ and μ_θ themselves. Therefore, in the frequency regime where the f^{-1} law is valid, μ is equal to $f S_{xx}(f)$ and can be directly obtained from figures 12(b) and 13(b). We find $\mu \approx 0.15$ and $\mu_\theta \approx 0.3$ in the NBL as well in the RL episodes. These results agree within a factor of two with values reported earlier and as reviewed by Sreenivasan & Kailasnath (1993). Note that in their review, Sreenivasan & Kailasnath (1993) discuss spectra and autocovariance functions of ε_r but they do not consider spectra or autocovariance functions of the *logarithm* of ε_r .

Using one of the evaluation methods described by Sreenivasan & Kailasnath (1993), Frehlich *et al.* (2004) find $\mu \approx 0.5$ and $\mu_\theta \approx 0.6$ from the data of the NBL episode. Frehlich *et al.*'s μ is twice as large as the value 0.25 that is considered quasi-universal by Sreenivasan & Kailasnath (1993). It has to be kept in mind, however, that practically all previously reported intermittency exponents have been measured either in the laboratory or in the atmospheric surface layer. In other words, very little is known about the intermittency exponents in the atmosphere in the stably stratified surface layer or above the surface layer.

7.4. *The power laws of the conditionally averaged temperature structure parameters*

In §3.1, we have shown that if $(C_\theta^2)_r$ and ε_r are jointly lognormally distributed, then the conditional average $\langle (C_\theta^2)_r | \varepsilon_r \rangle$ for a specified value of ε_r is proportional to ε_r^δ , where the exponent is $\delta = \rho_{xy}\sigma_y/\sigma_x - 1/3$ or, alternatively, $\delta = \rho_{xz}\sigma_z/\sigma_x$; see equations (4.8) and (4.12), respectively. Figures 8–11 show that the theoretical power-law models for $\langle (C_\theta^2)_r | \varepsilon_r \rangle$ agree quite well with the empirical conditional averages drawn from the four ensembles ‘all’, NBL, RL, and AD, respectively. At the tails of the ε_r distributions, the empirical conditional averages are typically smaller than the respective theoretical model. The reason is that mean values of a lognormally distributed population are negatively biased, and the bias increases with decreasing population size. Therefore, the $\langle (C_\theta^2)_r | \varepsilon_r \rangle$ bias has the largest magnitude in the tails of the ε_r population.

Figures 8–11 and table 1 show that δ is smaller (closer to 1/3) for the constant-altitude episodes NBL and RL and larger (closer to 2/3) for the episodes ‘all’ and AD, which contain samples from a wide variety of altitudes. This is consistent with the observation that the larger the ensemble size, the more closely the correlation coefficients ρ_{xy} and ρ_{xz} approach the value 1.

8. Summary and conclusions

Ten hours of high-resolution, kite-borne turbulence measurements in the lowest 500 m of the night-time troposphere over land have been analysed. Frequency spectra $S_{uu}(f)$ and $S_{\theta\theta}(f)$ of the wind speed and temperature fluctuations and frequency spectra $S_{xx}(f)$, $S_{yy}(f)$, $S_{zz}(f)$ of the logarithms of local dissipation rates and local temperature structure parameters have been presented. In addition, p.d.f.s and joint p.d.f.s of local dissipation rates, ε_r , and local temperature structure parameters, $(C_\theta^2)_r$, and conditionally averaged $(C_\theta^2)_r$ for specified values of ε_r have been evaluated. The main results are as follows:

(1) The ‘classical’ spectra $S_{uu}(f)$ and $S_{\theta\theta}(f)$ show two $-5/3$ regimes which are separated by a plateau. The high-frequency $-5/3$ regimes characterize three-dimensional, Kolmogorov-type small-scale turbulence; the low-frequency $-5/3$ regimes represent quasi-two-dimensional mesoscale motion, probably gravity waves. In ‘area-preserving’ representation, a deep spectral gap separates the two $-2/3$ regimes. The spectral plateau observed in the NBL comprises streamwise wavelengths between 230 m and 2.3 km.

(2) The ‘intermittency spectra’ $S_{xx}(f)$, $S_{yy}(f)$, $S_{zz}(f)$ also show plateaux separating two regimes in which the spectral densities decrease with increasing f . The plateaux in the intermittency spectra appear at the same frequencies as in the classical spectra. In this paper, the small-scale (high-frequency) variability in the intermittency spectra is referred to as small-scale intermittency, while the large-scale (low-frequency) variability in the intermittency spectra is called large-scale intermittency.

(3) At high frequencies, $S_{xx}(f)$, $S_{yy}(f)$, $S_{zz}(f)$ decrease proportionally to f^{-1} . It is analytically shown that $S_{xx}(f) = \mu f^{-1}$ follows from Kolmogorov’s (1962) lognormality hypothesis, $\sigma_x^2 = A + \mu \ln(L/r)$. That is, the (small-scale) intermittency exponents μ and μ_θ can be empirically determined from plots of $fS_{xx}(f)$ and $fS_{yy}(f)$, respectively.

(4) Conditional averages $\langle (C_\theta^2)_r | \varepsilon_r \rangle$ as functions of ε_r tend to be proportional to ε_r^δ , where the ‘logarithmic slope’ δ varies with the statistical ensemble. From four different ensembles, slopes between 0.38 (close to 1/3) and 0.72 (close to 2/3) are obtained. The two ensembles in which data were taken from a single altitude provided the smallest slopes, while the two ensembles that contained data from all altitudes provided the largest slopes. Two theoretical models, both of which provide power laws

for $\langle (C_\theta^2)_r | \varepsilon_r \rangle$, have been developed. The first model, referred to as the ‘small-scale intermittency model’, assumes that $(C_\theta^2)_r$ and ε_r are jointly lognormally distributed and leads to $\delta = \rho_{xy} \sigma_y / \sigma_x - 1/3$, where σ_x and σ_y are the standard deviations of the logarithms of ε_r and χ_r , and ρ_{xy} is the correlation coefficient between the logarithms of ε_r and χ_r . With the assumptions $\rho_{xy} \approx 2/3$ and $\sigma_y / \sigma_x \approx 1$ (Antonia & Van Atta 1975), the small-scale intermittency model leads to $\delta = 1/3$. An alternative model, referred to as the ‘large-scale intermittency model’, has been constructed on the basis of heuristic mixing-length arguments. With some not too restrictive additional assumptions, it leads to $\delta = 2/3$.

This study was supported by the National Science Foundation through grant ATM-0128089. In addition, A. M.’s contribution was supported by the US Army Research Office through grant DAAD 19-00-1-0527. Michael L. Jensen and Yannick Meillier were instrumental in collecting and archiving the measurements. The authors are grateful to Drs Robert Banta and Reginald Hill and to the anonymous reviewers for their comments and suggestions.

Appendix A. Conditional averages of jointly normally distributed variables

Consider the joint probability density function (p.d.f.) of two jointly normally distributed, zero-mean, unity-variance variables X and Y :

$$p_{XY}(X, Y) = \frac{1}{2\pi\sqrt{1-\rho^2}} \exp\left\{-\frac{X^2 - 2\rho XY + Y^2}{2(1-\rho^2)}\right\} \tag{A 1}$$

(Parzen 1960, p. 357), where ρ is the correlation coefficient of X and Y .

Now, let X be the (natural) logarithm of another random variable, x , such that

$$X = \frac{\ln(x/x_0)}{\sigma_X}, \tag{A 2}$$

where x_0 is chosen such that $\langle X \rangle = 0$, as was assumed. Correspondingly,

$$Y = \frac{\ln(y/y_0)}{\sigma_Y}. \tag{A 3}$$

Here, σ_X and σ_Y are the standard deviations of $\ln(x/x_0)$ and $\ln(y/y_0)$, respectively.

If the joint p.d.f. $p_{XY}(X, Y)$ of X and Y is jointly normal, then, by definition, $p_{xy}(x, y)$ (the joint p.d.f. of x and y) is jointly lognormal. The two joint p.d.f.s are connected through

$$p_{XY}(X, Y) dX dY = p_{xy}(x, y) dx dy. \tag{A 4}$$

Therefore,

$$p_{xy}(x, y) = \frac{1}{x_0 \sigma_X e^{\sigma_X X}} \frac{1}{y_0 \sigma_Y e^{\sigma_Y Y}} p_{XY}(X, Y). \tag{A 5}$$

Now, consider the conditional average of $x^a y^b$ for a specified value of x , where a and b are real numbers:

$$\langle x^a y^b | x \rangle \equiv \frac{\int_0^\infty p_{xy}(x, y) x^a y^b dy}{\int_0^\infty p_{xy}(x, y) dy} = x^a \langle y^b | y \rangle. \tag{A 6}$$

The integrations have to be performed between 0 and ∞ because lognormality of x and y implies that neither x nor y can assume negative values. The integrations can be conveniently carried out in logarithmic coordinates. With

$$y^b = e^{b\sigma_Y Y} y_0^b \tag{A 7}$$

and

$$dy = y_0 \sigma_Y e^{\sigma_Y Y} dY, \tag{A 8}$$

we find

$$\int_{x=0}^{\infty} p_{xy}(x, y) y^b dy = \frac{y_0^b}{x_0 \sigma_X} e^{-\sigma_X X} \int_{Y=-\infty}^{\infty} e^{b\sigma_Y Y} p_{XY}(X, Y) dY. \tag{A 9}$$

The remaining integral is of the form

$$\int_{-\infty}^{\infty} \exp(-\alpha Y^2 + \beta Y) dY = \sqrt{\frac{\pi}{\alpha}} \exp\left(\frac{\beta^2}{4\alpha}\right), \tag{A 10}$$

where

$$\alpha = \frac{1}{2(1 - \rho^2)} \tag{A 11}$$

and

$$\beta = b\sigma_Y + \frac{\rho}{1 - \rho^2} X. \tag{A 12}$$

Therefore,

$$\int_{x=0}^{\infty} p_{xy}(x, y) y^b dy = \sqrt{2\pi(1 - \rho^2)} \frac{y_0^b}{x_0 \sigma_X} e^{-\sigma_X X} \exp\left[\frac{1 - \rho^2}{2} \left(b\sigma_Y + \frac{\rho}{1 - \rho^2} X\right)^2\right]. \tag{A 13}$$

This leads to

$$\langle y^b | x \rangle = y_0^b \exp\left[\frac{1 - \rho^2}{2} b^2 \sigma_Y^2\right] \left(\frac{x}{x_0}\right)^{\rho b \sigma_Y / \sigma_X}. \tag{A 14}$$

With $\langle x^a y^b | x \rangle = x^a \langle y^b | x \rangle$, we find

$$\langle x^a y^b | x \rangle = y_0^b \exp\left[\frac{1 - \rho^2}{2} b^2 \sigma_Y^2\right] x^a \left(\frac{x}{x_0}\right)^{\rho b \sigma_Y / \sigma_X}. \tag{A 15}$$

That is, if x and y are jointly lognormal, then $\langle x^a y^b | x \rangle$ as a function of x is a power law,

$$\langle x^a y^b | x \rangle = c x^\delta, \tag{A 16}$$

with the coefficient

$$c = x_0^{-\rho b \sigma_Y / \sigma_X} y_0^b \exp\left[\frac{1 - \rho^2}{2} b^2 \sigma_Y^2\right] \tag{A 17}$$

and the exponent, or ‘logarithmic slope’,

$$\delta = a + \rho b \frac{\sigma_Y}{\sigma_X}. \tag{A 18}$$

Appendix B. Relationships between variances and correlation coefficients of the logarithms of ε_r , χ_r , and $(C_\theta^2)_r$

Consider the random variable

$$z = ax + by, \tag{B 1}$$

where a and b are constant real numbers and x and y are zero-mean random variables with a correlation coefficient

$$\rho_{xy} = \frac{\langle xy \rangle}{\sigma_x \sigma_y}, \tag{B 2}$$

where $\sigma_x^2 \equiv \langle x^2 \rangle$ and $\sigma_y^2 \equiv \langle y^2 \rangle$ are the variances of x and y , respectively.

By definition, the correlation coefficient of x and z is

$$\rho_{xz} = \frac{\langle xz \rangle}{\sqrt{\langle x^2 \rangle \langle z^2 \rangle}} = \frac{a \langle x^2 \rangle + b \langle xy \rangle}{\sqrt{\langle x^2 \rangle (a^2 \langle x^2 \rangle + 2ab \langle xy \rangle + b^2 \langle y^2 \rangle)}}, \tag{B 3}$$

which gives

$$\rho_{xz} = \frac{a + b\rho_{xy}\sigma_y/\sigma_x}{\sqrt{a^2 + 2ab\rho_{xy}\sigma_y/\sigma_x + b^2\sigma_y^2/\sigma_x^2}}. \tag{B 4}$$

In addition, we can express the variance $\sigma_z^2 \equiv \langle z^2 \rangle$ in terms of σ_x and σ_y :

$$\sigma_z^2 = a^2\sigma_x^2 + 2ab\rho_{xz}\sigma_x\sigma_y + b^2\sigma_y^2. \tag{B 5}$$

Now, consider the case where

$$x = \ln \frac{\varepsilon_r}{\overline{\varepsilon_r}}, \tag{B 6}$$

$$y = \ln \frac{\chi_r}{\overline{\chi_r}} \tag{B 7}$$

and

$$z = \ln \frac{(C_\theta^2)_r}{\overline{(C_\theta^2)_r}}. \tag{B 8}$$

Here, $\overline{\varepsilon_r}$, $\overline{\chi_r}$, and $\overline{(C_\theta^2)_r}$ are the ‘geometric mean values’ (Obukhov 1962, p. 79) of ε_r , χ_r , and $(C_\theta^2)_r$, respectively, such that x , y , and z are indeed zero-mean variables. Through the Obukhov–Corrsin relation,

$$(C_\theta^2)_r = \gamma \varepsilon_r^{-1/3} \chi_r, \tag{B 9}$$

we find

$$a = -\frac{1}{3} \tag{B 10}$$

and

$$b = 1. \tag{B 11}$$

This leads to

$$\rho_{xz} = \frac{-\frac{1}{3} + \rho_{xy}\sigma_y/\sigma_x}{\sqrt{\frac{1}{9} - \frac{2}{3}\rho_{xy}\sigma_y/\sigma_x + \sigma_y^2/\sigma_x^2}} \tag{B 12}$$

and

$$\sigma_z^2 = \frac{1}{9}\sigma_x^2 - \frac{2}{3}\rho_{xy}\sigma_x\sigma_y + \sigma_y^2. \tag{B 13}$$

These two equations, (B 12) and (B 13), relate five quantities with each other: the three standard deviations σ_x , σ_y , and σ_z , and the two correlation coefficients ρ_{xy} and ρ_{xz} . Three of these five, namely σ_x , σ_z , and ρ_{xz} , can be measured with fine wires operating in the inertial range. The other two, σ_y and ρ_{xy} , can be directly measured only if the dissipation scales are resolved. But σ_y and ρ_{xy} can still be retrieved from inertial-range measurements of σ_x , σ_z , and ρ_{xz} . From $y = (z - ax)/b$ we find

$$\sigma_y^2 = \frac{a^2}{b^2}\sigma_x^2 - 2\frac{a}{b^2}\rho_{xz}\sigma_x\sigma_z + \frac{1}{b^2}\sigma_z^2 \quad (\text{B } 14)$$

and

$$\rho_{xy} = \frac{-(a/b)\sigma_x^2 + (1/b)\rho_{xz}\sigma_x\sigma_z}{\sigma_x\sqrt{(a^2/b^2)\sigma_x^2 - 2(a/b^2)\rho_{xz}\sigma_x\sigma_z + (1/b^2)\sigma_z^2}}. \quad (\text{B } 15)$$

With $a = -1/3$ and $b = 1$, this leads to

$$\sigma_y^2 = \frac{1}{9}\sigma_x^2 + \frac{2}{3}\rho_{xz}\sigma_x\sigma_z + \sigma_z^2 \quad (\text{B } 16)$$

and

$$\rho_{xy} = \frac{\sigma_x + 3\rho_{xz}\sigma_z}{\sqrt{\sigma_x^2 + 6\rho_{xz}\sigma_x\sigma_z + 9\sigma_z^2}}. \quad (\text{B } 17)$$

Note that in this Appendix, no assumptions on the p.d.f.s or joint p.d.f.s of x , y , and z , or of ε_r , χ_r , and $(C_\theta^2)_r$, have been made.

REFERENCES

- ANTONIA, R. A. & VAN ATTA, C. W. 1975 On the correlation between temperature and velocity dissipation fields in a heated turbulent jet. *J. Fluid Mech.* **67**, 273–288.
- BALSLEY, B. B., JENSEN, M. L. & FREHLICH, R. G. 1998 The use of state-of-the-art kites for profiling the lower atmosphere. *Boundary-Layer Met.* **87**, 1–25.
- BALSLEY, B. B., JENSEN, M. L., FREHLICH, R. G., MEILLIER, Y. & MUSCHINSKI, A. 2003 Extreme gradients in the nocturnal boundary layer: structure, evolution, and potential causes. *J. Atmos. Sci.* **60**, 2496–2508.
- BATCHELOR, G. K. & TOWNSEND, A. A. 1949 The nature of turbulent motion at high wave-numbers. *Proc. R. Soc. Lond. A* **199**, 238–255.
- BOETTCHER, F., RENNER, C., WALDL, H.-P. & PEINKE, J. 2003 On the statistics of wind gusts. *Boundary-Layer Met.* **108**, 163–173.
- CHO, J. Y. N. & LINDBORG, E. 2001 Horizontal velocity structure functions in the upper troposphere and lower stratosphere. 1. Observations. *J. Geophys. Res.* **106**, 10223–10232.
- CORRSIN, S. 1951 On the spectrum of isotropic temperature fluctuations in an isotropic turbulence. *J. Appl. Phys.* **22**, 469–473.
- DAVENPORT & ROOT 1958 *Random Signals and Noise*. McGraw-Hill.
- DOVIK, R. J. & ZRNIC, D. S. 1993 *Doppler Radar and Weather Observations*, 2nd Edn. Academic.
- FIEDLER, F. & PANOFKY, H. A. 1970 Atmospheric scales and spectral gaps. *Bull. Am. Met. Soc.* **51**, 1114–1119.
- FREHLICH, R. G. 1992 Laser scintillation measurements of the temperature spectrum in the atmospheric surface layer. *J. Atmos. Sci.* **49**, 1494–1509.
- FREHLICH, R. G., MEILLIER, Y., JENSEN, M. L. & BALSLEY, B. B. 2003 Turbulence measurements with the CIRES Tethered Lifting System during CASES-99: calibration and spectral analysis of temperature and velocity. *J. Atmos. Sci.* **60**, 2487–2495.
- FREHLICH, R. G., MEILLIER, Y., JENSEN, M. L. & BALSLEY, B. B. 2004 A statistical description of small-scale turbulence in the low-level nocturnal jet. *J. Atmos. Sci.* **61**, 1079–1085.
- FRITTS, D. C. & RASTOGI, P. K. 1985 Convective and dynamical instabilities due to gravity wave motions in the lower and middle atmosphere: Theory and observations. *Radio Sci.* **20**, 1247–1277.

- GAGE, K. S. 1979 Evidence of a $k^{-5/3}$ law inertial range in mesoscale two-dimensional turbulence. *J. Atmos. Sci.* **36**, 1950–1954.
- GAGE, K. S. 1990 Radar observations of the free atmosphere: structure and dynamics. In *Radar in Meteorology* (ed. D. Atlas), pp. 534–565. Am. Met. Soc.
- GOTOH, T., FUKAYAMA, D. & NAKANO, T. 2002 Velocity field statistics in homogeneous steady turbulence obtained using a high-resolution direct numerical simulation. *Phys. Fluids* **14**, 1065–1081.
- HESKESTAD, G. 1965 A generalized Taylor hypothesis with application for high Reynolds number turbulent shear flows. *J. Appl. Mech.* **87**, 735–739.
- HILL, R. J. 1978 Models of the scalar spectrum for turbulent advection. *J. Fluid Mech.* **88**, 541–562.
- HILL, R. J. 1996 Corrections to Taylor's frozen turbulence approximation. *Atmos. Res.* **40**, 153–175.
- HILL, R. J. & WILCZAK, J. M. 2001 Fourth-order velocity statistics. *Fluid Dyn. Res.* **28**, 1–22.
- KOLMOGOROV, A. N. 1941 Local structure of turbulence in an incompressible fluid at very high Reynolds numbers. *Dokl. Akad. Nauk SSSR* **30**, 299–303.
- KOLMOGOROV, A. N. 1962 A refinement of previous hypotheses concerning the local structure of turbulence in a viscous incompressible fluid at high Reynolds number. *J. Fluid Mech.* **13**, 82–85.
- KRAICHNAN, R. H. 1967 Inertial ranges in two-dimensional turbulence. *Phys. Fluids* **10**, 1417–1423.
- KUZNETSOV, V. R., PRASKOVSKY, A. A. & SABELNIKOV, V. A. 1992 Fine-scale turbulence structure of intermittent shear flows. *J. Fluid Mech.* **234**, 595–622.
- LILLY, D. K. 1983 Stratified turbulence and the mesoscale variability of the atmosphere. *J. Atmos. Sci.* **40**, 749–761.
- LINDBORG, E. & CHO, J. Y. N. 2001 Horizontal velocity structure functions in the upper troposphere and lower stratosphere. 2. Theoretical considerations. *J. Geophys. Res.* **106**, 10233–10241.
- LUMLEY, J. L. 1965 Interpretation of time spectra measured in high-intensity shear flows. *Phys. Fluids* **8**, 1056–1062.
- LUMLEY, J. L. & PANOFSKY, H. A. 1964 *The Structure of Atmospheric Turbulence*. Wiley Interscience.
- MAHRT, L. 1989 Intermittency of atmospheric turbulence. *J. Atmos. Sci.* **46**, 79–95.
- MAHRT, L., MOORE, E. & VICKERS, D. 2001 Dependence of turbulence and mesoscale velocity variances on scale and stability. *J. Appl. Met.* **40**, 628–641.
- MONIN, A. S. & YAGLOM, A. M. 1975 *Statistical Fluid Mechanics, Vol. II*. The MIT Press.
- MUSCHINSKI, A. 1996 A similarity theory of locally homogeneous and isotropic turbulence generated by a Smagorinsky-type LES. *J. Fluid Mech.* **325**, 239–260.
- MUSCHINSKI, A. 2004 Local and global statistics of clear-air Doppler radar signals. *Radio Sci.* **39**, RS1008, doi:10.1029/2003RS002908.
- MUSCHINSKI, A., FREHLICH, R., JENSEN, M., HUGO, R., HOFF, A., EATON, F. & BALSLEY, B. 2001 Fine-scale measurements of turbulence in the lower troposphere: an intercomparison between a kite- and balloon-borne, and a helicopter-borne measurement system. *Boundary-Layer Met.* **98**, 219–250.
- MUSCHINSKI, A. & LENSCHOW, D. H. 2001 Future directions for research on meter- and submeter-scale, atmospheric turbulence. *Bull. Am. Met. Soc.* **82**, 2831–2843.
- MUSCHINSKI, A. & ROTH, R. 1993 A local interpretation of Heisenberg's transfer theory. *Contr. Atmos. Phys.* **66**, 335–346.
- NASTROM, G. D. & EATON, F. D. 1997 Turbulence eddy dissipation rates from radar observations at 5–20 km at White Sands Missile Range, New Mexico. *J. Geophys. Res.* **102**, 19495–19505.
- NASTROM, G. D. & GAGE, K. S. 1985 A climatology of atmospheric wavenumber spectra of wind and temperature observed by commercial aircraft. *J. Atmos. Sci.* **42**, 950–960.
- OBUKHOV, A. M. 1941a Spectral energy distribution in a turbulent flow. *Dokl. Akad. Nauk SSSR* **32**, 22–24.
- OBUKHOV, A. M. 1941b Spectral energy distribution in a turbulent flow. *Izv. Akad. Nauk SSSR, Ser. Geogr. i Geofiz.* **5**, 453–466.
- OBUKHOV, A. M. 1949 The structure of the temperature field in a turbulent flow. *Izv. Akad. Nauk SSSR, Ser. Geogr. i Geofiz.* **13**, 58–69.
- OBUKHOV, A. M. 1962 Some specific features of atmospheric turbulence. *J. Fluid Mech.* **13**, 77–81.
- OZMIDOV, R. V. 1965 Energy distribution between oceanic motions of different scales. *Izv. Akad. Nauk SSSR, Fiz. Atmos. Okeana* **1**, 439–448.

- PARZEN, E. 1960 *Modern Probability Theory and its Applications*. John Wiley & Sons.
- PELTIER, L. J. & WYNGAARD, J. C. 1995 Structure-function parameters in the convective boundary layer from large-eddy simulation. *J. Atmos. Sci.* **52**, 3641–3660.
- POULOS, G. S., BLUMEN, W., FRITTS, D. C., LUNDQUIST, J. K., SUN, J., BURNS, S. P., NAPPO, C., BANTA, R., NEWSOM, R., CUXART, J., TERRADELLAS, E., BALSLEY, B. & JENSEN, M. 2002 CASES-99: A comprehensive investigation of the stable nocturnal boundary layer. *Bull. Am. Met. Soc.* **83**, 555–581.
- PRANDTL, L. 1925 Bericht über Untersuchungen zur ausgebildeten Turbulenz. *Z. Angew. Math. Mech.* pp. 136–139.
- PRASKOVSKY, A. A., GLEDZER, E. B., KARYAKIN, M. Y. & ZHOU, Y. 1993 The sweeping decorrelation hypothesis and energy-inertial scale interaction in high Reynolds number flows. *J. Fluid Mech.* **248**, 493–511.
- SMITH, K. S. 2004 Comments on “The k^{-3} and $k^{-5/3}$ energy spectrum of atmospheric turbulence: Quasigeostrophic two-level model simulation”. *J. Atmos. Sci.* **61**, 937–942.
- SREENIVASAN, K. R. 1995 On the universality of the Kolmogorov constant. *Phys. Fluids* **7**, 2778–2784.
- SREENIVASAN, K. R. 1996 The passive scalar spectrum and the Obukhov-Corrsin constant. *Phys. Fluids* **8**, 189–196.
- SREENIVASAN, K. R. 1999 Fluid turbulence. *Rev. Mod. Phys.* **71**, S383–S395.
- SREENIVASAN, K. R. & ANTONIA, R. A. 1997 The phenomenology of small-scale turbulence. *Annu. Rev. Fluid Mech.* **29**, 435–472.
- SREENIVASAN, K. R., ANTONIA, R. A. & DANH, H. Q. 1977 Temperature dissipation fluctuations in a turbulent boundary layer. *Phys. Fluids* **20**, 1238–1249.
- SREENIVASAN, K. R. & KAILASNATH, P. 1993 An update on the intermittency exponent in turbulence. *Phys. Fluids A* **5**, 512–514.
- TATARSKII, V. I. 1961 *Wave Propagation in a Turbulent Medium*. McGraw-Hill.
- TAYLOR, G. I. 1935 Statistical theory of turbulence. *Proc. R. Soc. Lond. A* **151**, 421–478.
- TAYLOR, G. I. 1938 The spectrum of turbulence. *Proc. R. Soc. Lond. A* **164**, 476–490.
- TENNEKES, H. 1975 Eulerian and Lagrangian time microscales in isotropic turbulence. *J. Fluid Mech.* **67**, 561–567.
- TREVIÑO, G. & ANDREAS, E. L. 2000 Averaging intervals for spectral analysis of nonstationary turbulence. *Boundary-Layer Met.* **95**, 231–247.
- TUNG, K. K. 2004 Reply. *J. Atmos. Sci.* **61**, 943–948.
- TUNG, K. K. & ORLANDO, W. W. 2003 The k^{-3} and $k^{-5/3}$ energy spectrum of atmospheric turbulence: Quasigeostrophic two-level model simulation. *J. Atmos. Sci.* **60**, 824–835.
- VAN ATTA, C. W. 1971 Influence of fluctuations in local dissipation rates on turbulent scalar characteristics in the inertial subrange. *Phys. Fluids* **14**, 1803–1804.
- VAN DER HOEVEN, I. 1957 Power spectrum of horizontal wind speed in the frequency range from 0.0007 to 900 cycles per hour. *J. Met.* **14**, 160–164.
- VANZANDT, T. E., GREEN, J. L., GAGE, K. S. & CLARK, W. L. 1978 Vertical profiles of refractivity turbulence structure constant: Comparison of observations by the Sunset radar with a new theoretical model. *Radio Sci.* **13**, 819–829.
- VICKERS, D. & MAHRT, L. 2003 The cospectral gap and turbulent flux calculations. *J. Atmos. Oceanic Technol.* **20**, 660–672.
- WARHAFT, Z. 2000 Passive scalars in turbulent flows. *Annu. Rev. Fluid Mech.* **32**, 203–240.
- WHEELON, A. D. 2001 *Electromagnetic Scintillation. I. Geometrical Optics*. Cambridge University Press.
- WHEELON, A. D. 2003 *Electromagnetic Scintillation. II. Weak Scattering*. Cambridge University Press.
- WYNGAARD, J. C. & CLIFFORD, S. F. 1977 Taylor’s hypothesis and high-frequency turbulence spectra. *J. Atmos. Sci.* **34**, 922–929.
- YAGLOM, A. M. 1981 Laws of small-scale turbulence in atmosphere and ocean (in commemoration of the 40th anniversary of the theory of locally isotropic turbulence). *Izv. Atmos. Ocean. Phys.* **17**, 919–935.